Two-Color Ultrafast Yb:Fiber Chirped Pulse Amplifier for Mid-Infrared Generation and Sensitive Mid-Infrared Detector Based on Extreme Non-Degenerate Two Photon Absorption in GaAs

by

Siyuan Bian

A thesis

presented to the University of Waterloo

in fulfilment of the

thesis requirement for the degree of

Master of Science

in

Physics

Waterloo, Ontario, Canada, 2014

I hereby declare that I am the sole author of this thesis. This is a true copy of the thesis, including any required final revisions, as accepted by my examiners.

I understand that my thesis may be made electronically available to the public.

Abstract

This thesis outlines the development and optimization of a two-color three-stage ultrafast Yb:fiber chirped pulse amplifier for the generation of mid-infrared (MIR) radiation and a novel sensitive mid-infrared detector by using extreme non-degenerate two photon absorption (END-TPA) technique in GaAs. The two amplified colors used to generate MIR by difference frequency generation are centered at 1038nm and 1103nm respectively. The two colors are generated by continuum generation in a photonic crystal fiber pumped by a mode-locked Yb:fiber laser. One of the main goals of this thesis is to improve the power of the two colors to improve the MIR generation efficiency, because the difference frequency nonlinear mixing is proportional to the product of the power of the input colors. Towards this goal, we developed a three-stage Yb:fiber chirped pulse amplifier system that can generate more powerful MIR radiation compared with our previous two-stage system. In this thesis, approximately 65nm of wavelength separation between the two colors centered at 1038nm and 1103nm is accomplished through our pre-amplifier and two main amplifiers. The maximum combined average power is 2.65W after the last amplifier. A three-grating compressor is then used to compress the two colors to around 600fs and 1ps pulse durations and the average power of two colors is reduced to 1.86W after the compressor. By applying difference frequency generation in a 1-mm-thick GaSe crystal, 1.7mW average power, short-pulse MIR radiation is achieved.

In this research, another important goal is to develop a sensitive MIR radiation detector based on END-TPA. It is well known that when the total photon energies of two photons exceed the energy band-gap of a semiconductor, the two photons will be absorbed simultaneously. More recently, it has been shown that if there is an extremely large difference between the frequencies of the two incident photons there can be a large increase in the two-photon absorption coefficient. Our goal is to demonstrate END-TPA in GaAs with the generated 17.6μm MIR radiation pulses and 920nm pulses that are generated in the continuum produced in the photonic crystal fiber. The two pulses are temporally and spatially overlapped onto a GaAs detector. This END-TPA detector could then be used to measure the pulse duration of the ultra-short MIR pulse based by cross-correlation of the MIR and 920nm pulses.

Acknowledgements

First of all, I would like to thank my supervisor Dr. Donna Strickland for offering me the great opportunity to work in her research lab and the help and guidance on my research project.

I also wish to thank Dr. Li Wei, Dr.Kostadinka Bizheva, and Dr. Donna Strickland for being my thesis defense committee. I also wish to thank Dr. Joe Sanderson for being my master-committing member in the last two years.

Finally, I would like to thank my father and my mother for their support and encouragements.

Table of Content

List of Figures

1. Introduction

Since the first laser launched in 1960, developments have been made to improve the performance of lasers with shorter pulses and higher intensity. Recently, laser sources delivering ultra-short pulses at the MIR wavelength region of 5μm-20μm have attracted great interest due to their applications in many scientific and industrial areas (Ebrahim-Zadeh, 2008). Because many organic molecules exhibit vibration bands in the MIR spectral region, ultra-short MIR laser sources can also be used to image and control molecular motion. Due to all those applications, it is important to generate high-intensity MIR pulses. In this thesis, we developed a three-stage Yb:fiber chirped pulse amplifier (CPA) system for MIR generation. Compared with our previous two-stage Yb:fiber CPA system, this new system generates more intensity MIR pulses around 17μm by difference frequency mixing two colors centered at 1038nm and 1103nm respectively. Based on our previous experimental setup, it is impossible to measure the exact pulse duration of MIR. However, a novel sensitive detector has been set up in my experiment not only to detect MIR pulses, but also to measure the pulse duration of that by applying the END-TPA in GaAs.

1.1 Two-Color Yb:Fiber CPA for Mid-Infrared Generation

Though many laser materials have been discovered with broad gain spectrum, most lasers still operate at the visible and near IR wavelength region. Because of the lack of suitable laser materials, there is still a limitation of laser gain medium at the MIR spectral region. However, nonlinear optical (NLO) techniques offer us various frequency- down-conversion schemes, and the most conventional one is difference frequency generation (DFG) due to its simple geometry. In the frequency-down-conversion process, two optical pulses referred to as the pump and the signal, with frequencies ω_p, and ω_s, respectively, are interacting with each other in a NLO crystal and the process induces another oscillation with frequency $\omega_p - \omega_s$, which is referred to as the idler frequency. From energy conservation, one atom in the NLO crystal is excited to the highest virtual energy level, and then it decays from that energy level to another virtual energy level and finally to the ground state. This process results in the emission of signal and idler photons. The generated frequency ω_i is in the MIR spectral region and this generation process for MIR pulses under the collinear condition can be generally depicted as in Figure 1-1.
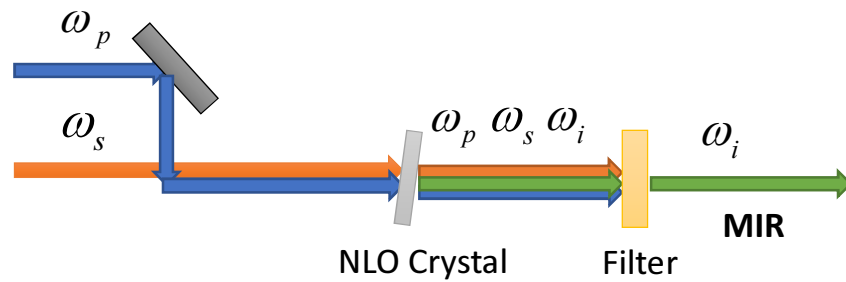
Figure 1-1 MIR pulses generation based on DFG.

The DFG technique requires two synchronized light pulses with the required spectral spacing for the pump and signal wavelengths for generation of MIR pulses at the desired idler wavelength. Moreover, tunable two colors or tunable dual wavelengths are preferable because they can generate tunable MIR pulses for many scientific and industrial applications. It is well known that the power of the MIR radiation generated by DFG of dual wavelengths is proportional to the product of the two input intensities. Thus, to achieve ultra-short intense two colors with proper wavelengths is the most important goal for generating ultra-short MIR radiation. A number of approaches are being explored to reach this goal.

High intensity pulse propagation in materials can produce a strong Kerr effect, which causes the index of refraction of materials to be dependent on the intensity of light. This nonlinear effect will induce the self-focusing of the beam in the materials, and the increased intensity associated with the self-focused beam can easily exceed the damage threshold of the amplifier materials (Weiner, 2011). To overcome the intensity limitation, in 1985, an approach known as Chirped Pulse Amplification (CPA), for ultra-short laser amplifiers was invented by Donna Strickland and Gerard Mourou (Strickland, 1985). This idea can be sketched in Figure 1-2. In the CPA system, ultra-short pulses are passed through a dispersive system such as grating pairs or fibers, leading to temporal stretching of the laser pulses. The peak intensity of the laser pulse is reduced to a safe amount, as the envelope of the pulse has been stretched due to the group delay dispersion. Then the stretched pulses are amplified in the amplifier material through either a single or a multi-stage amplifier design. After amplification, the laser pulses are compressed by using grating pairs (Treacy, 1969). The CPA technique for ultra-short lasers not only overcomes self-focusing and laser damage problems in solid state lasers, but also avoids self-phase modulation of laser pulses in fibers.
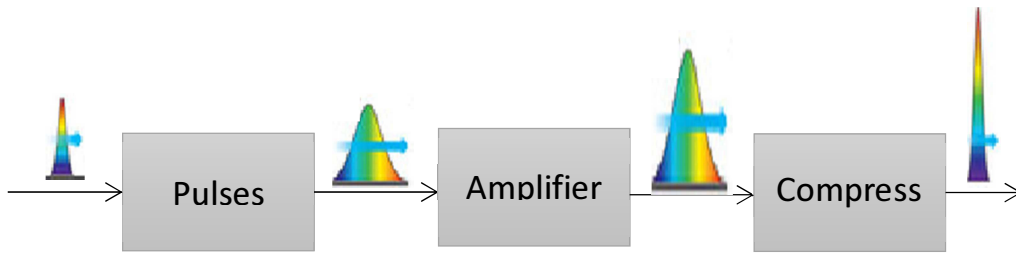
Figure 1-2 The chirped pulse amplification technique.

One common method to generate ultra-short MIR radiation is using the signal and idler wavelengths of an optical parametric oscillator (OPO) as dual wavelengths for difference frequency mixing. In an OPO system, intense laser pulses interact with the in-cavity NLO crystal in the OPO cavity, both the signal and idler pulses can be generated. By changing the OPO cavity length, tunable wavelengths of signal and idler pulses can be obtained (Dunn, 1999). Based on this OPO-DFG system, Ehret and Schnieder applied an intense laser system consisting of a mode-locked Ti: sapphire laser (output power 2.3W) pumping the OPO system, and generated dual wavelengths ranging from 1.35μm to 1.6μm and from 2.05μm to 1.65μm respectively. The sub-picosecond MIR pulses with tunable wavelength region from 5.2μm to 18μm were achieved by difference frequency generation in a 1mm GaSe crystal (Ehret, 1998). The average power they obtained was about 100μW in the wavelengths 16-18μm with a repetition rate of 76MHz. In 2012, Hegenbarth et. al. reported a MIR radiation up to 4.3mW average power at a repetition of 42MHz (Hegenbarth, 2012). The peak wavelength of the MIR radiation was tunable between 10.5μm and 16.5μm. As referred to their dual-wavelength generation system, the OPO delivers up to 1.4W mixing power at two different wavelengths, ranging from 1563nm to 1621nm and from 1795nm to 1859nm respectively.

Recently, with the help of CPA technology, Yb:fiber CPA laser system with high intensity has been demonstrated by Galvanauskas et. al. (Galvanauskas, 2001). In their experiments, Yb-doped glass fibers with broad band wavelength range from 975nm to 1200nm (Paschotta, 1997) are preferable, for their pumping efficiency is higher than that of Er-doped fibers. Due to the known advantages of Yb:fibers CPA lasers such as low cost, high intensity, and ease of thermal management, Yb:fiber-based MIR generation systems could be the most practical MIR sources. In the dual-wavelength Yb:fiber CPA system, the required two colors are amplified from the seed, which is selected from a PCF super continuum or from two synchronized diode lasers. However, the drawback of this process is the production of amplified spontaneous emission (ASE) induced in the pumped Yb:fibers. It is generated initially from the spontaneous emission in the fiber. When the pump power becomes high,

the spontaneous emission itself can promote simulated emission, and becomes amplified. Thus, the ASE becomes very strong at the output end of the highly pumped fiber with a long length. It is an unwanted effect in fiber amplification as it will compete with the input seed and deplete the gain. This problem can usually be controlled by sending more powerful seeding into the fiber, because the stronger seeding can extract more gain and so supress the ASE in the amplifier system.

In the previous work, R. Romero Alvarez et. al. developed a two-color Yb:fiber amplifier and generated the two colors with the peak wavelengths centered at 1039nm and 1103nm respectively (Romero-Alvarez, 2008). Based on these dual wavelengths, a MIR radiation with an average power of 20μW centered at 18μm was generated using a 1mm GaSe crystal as the NLO crystal. In order to achieve a more efficient fiber amplifier system, a pre-amplifier was applied in fiber CPA system by Al-Kadry and Donna Strickland in 2011 (Al-Kadry, 2011). They used a 2m single-mode single-clad Yb:fiber pumped at both ends for the pre-amplifier. With this pre-amplifier, the two colors could extract gain more efficiently in the main amplifier stage, resulting of total power 1.1W at the output after the main amplifier. The power of the two colors was much higher than that in the previous work, because the two-color seed power was high enough to compete with the ASE induced in the main amplifier and so the seed was amplified more efficiently. By difference frequency mixing these two powerful colors, MIR radiation centred at 17.5μm with an average power of 400μW was generated. Then the fiber lengths of the pre-amplifier and the main amplifier were optimized by Hajialamdari (Hajialamdari, 2012). According to his work, the optimum fiber lengths of the pre-amplifier and the main amplifier are 7.5m and 10.5m respectively. The pre-amplifier was still using a single-mode single-clad Yb:fiber and the main amplifier applied a double-clad, highly-doped Yb:fiber. Moreover, the pre-amplifier was co-pumped by a diode laser with a maximum output power of 350mW and was counter-pumped by a diode laser with a maximum output power of 500mW. The output power after the pre-amplifier had been improved by one order of magnitude compared with that in the previous work. Based on this new two-stage Yb:fiber amplifier system, Hajialamdari not only further increased the wavelength separation between the two colors, but also made it a tunable two-color Yb:fiber CPA for MIR generation. They recorded an average power up to 1.5mW at 18μm corresponding to the two colors with the peak wavelengths of 1040nm and 1103nm and average power of 1350mW and 80mW respectively. This ultra-short Yb:fiber CPA could also generate tunable MIR radiation within the spectral region from 16μm to 20μm with an average power of 0.8mW.

In my thesis, two aspects need to be improved based on the previous two-stage Yb:fiber CPA system. One is to further extend the spectral separation between the two colors in order to generate a MIR radiation with the peak wavelength smaller than 16μm. It is well known that the absorption and gain spectral regions of Yb doped fiber range from 850nm to 1150nm and from 900nm to 1150nm respectively. In a short-length fiber, if we shift the blue color (the shorter wavelength seed) towards the blue-color side, the peak wavelength of the blue color will be closer to the gain peak, resulting of more gain extracted by the short-wavelength seed. Thus, the red-color seed is hard to extract enough gain to be amplified in the fibers. The product of the two color intensity will be reduced and the intensity of generated MIR radiation will be reduced too. Considering the competition of the two colors in our fibers, the best way to obtain further separation is to shift the long-wavelength seed towards the red-color side. However, the emission cross-section or the gain in the long-wavelength side is really low, which means it will also decrease the intensity of our amplified red color. In order to further separate the two colors but without reducing the intensity of the them, we can develop a three-stage Yb:fiber CPA system to amplify the weak red-color seed. Another goal of my thesis is to increase the intensity of the MIR pulses. Compared with the previous system, a three-stage Yb:fiber CPA system with one more amplifier stage can generate the two colors with more intensity. Consequently, both aspects can be improved by applying a three-stage Yb:fiber CPA system.

In my experiment, our group has developed a more complicated three-stage Yb:fiber CPA for MIR generation. A single-mode single-clad fiber is still used in the pre-amplifier, while two double-clad, highly-doped fibers with different lengths are used in the second and the third amplifiers. The generated MIR radiation is 1.7mW at 17.6μm corresponding to the two colors with the peak wavelengths of 1038nm and 1103nm and average power of 1780mW and 80mW respectively. This result is higher than that obtained in the previous work at the same wavelength. In addition, the large spectral bandwidth and the strong power of the two colors allow this system to further separate the two colors and generate the MIR radiation with a peak wavelength smaller than 16μm.

1.2   Sensitive Mid-Infrared Detector Based on END-TPA

Two-photon absorption is simultaneous absorption of two photons with identical or different photon energies, resulting in an excitation of an atom or a molecule from the ground state to a higher energy state. Actually, one of the incident photons promotes the molecule into a virtual state between the ground state and the excited state, then another photon will be absorbed by the molecule and the

molecule will jump into the final excited state. The TPA process is a nonlinear process therefore the absorption rate is proportional to the product of the intensities of the incident pulses. Compared with linear one photon absorption, the absorption coefficient of TPA is much smaller. However, the development of intense lasers has largely increased the TPA effect.

In homogeneous media, the TPA process arises from the imaginary part of the third-order nonlinear susceptibility (Boyd, 2008). Due to the large third-order nonlinearities in semiconductors, TPA in semiconductors has been extensively studied. The degenerate TPA was first studied. In order to scale the absorption coefficient of two identical incident photons, Wherrett applied the simplest two degenerate parabolic-band-structure assumption to roughly obtain the TPA coefficient and found this coefficient was inversely proportional to the E_g^3 of the semiconductor (Wherrett, 1984). The relation between the TPA coefficient and the band-gap energy was then proven in various semiconductors with different band-gap energy by Stryland (Van Stryland, 1985). Based on their results, the degenerate TPA (D-TPA) coefficient is very small in wide band-gap semiconductors. In order to obtain larger TPA coefficients even in wide band-gap semiconductors, non-degenerate (ND-TPA) and extreme non-degenerate (END-TPA) were processed in some semiconductors (Fishman, 2011). In their experiments, they reported a large enhancement of TPA using END-TPA and demonstrated TPA enhancements by factors of 100-1000 over D-TPA in direct-band-gap semiconductors. A femtosecond END-TPA experiment was set up in their work by sending one pulse with peak wavelength of 5.6μm and another one with peak wavelength of 390nm into a GaN diode. By increasing the intensity of the 390nm pulse up to 3.2GW cm^{-2}, the output voltage from the GaN diode was shown higher than that from a Mercury Cadmium Telluride (MCT) detector for detecting the 5.6μm pulse. Based on this experimental result, a novel setup was developed to be a sensitive detector for MIR radiation.

In my experiment, I set up the probe-pump END-TPA scheme for detecting our MIR radiation with the peak wavelength at 17.6μm. Pulses centered on 920nm were sent to a GaAs (E_g=1.42eV) diode temporally and spatially together with the MIR radiation generated in our three-stage Yb:fiber CPA system. This larger difference in wavelength is theoretically predicted to lead to larger enhancements in TPA (Cirloganu, 2011), and our setup would prove that prediction by experiments. Moreover, this sensitive detector of MIR radiation can be also used to measure the time duration of the MIR pulse. One translation stage can be used in the optical path of 920nm pulses to create a time delay between the MIR pulse and the 920nm pulse, and the pulse duration of the MIR radiation can be

easily measured by applying the cross-correlation method. However, in previous works, the temporal durations of all the generated MIR pulses can be just estimated by assuming these pulses are perfectly transform limited, Gaussian-shape pulses.

1.3   Outline of This Thesis

In this thesis, five chapters are organized in order: Introduction, Theoretical Background, Experimental Setup and Procedures, Experimental Results and Discussion, and Conclusion. Chapter 2 includes both the theories of noise equivalent power in Yb:fiber amplifiers and END-TPA in direct-band semiconductors. Noise equivalent power is used to explain the competition of our two-color seed and the amplified spontaneous emission in the fiber amplifiers. Then in the second part of Chapter 2, the absorption coefficient of TPA in semiconductors will be introduced and a novel method of MIR detector based on END-TPA is also explained. In Chapter 3, different components in our three-stage Yb:fiber CPA system are presented step by step. It also includes a comparison between different pumping geometries as well as different combinations of fibers in our whole system. In addition, Chapter 3 also presents the experimental setup of the conventional MIR detector and our novel MIR detector based on END-TPA. Chapter 4 discuss all the results obtained during our experiment and Chapter 5 includes the conclusion for this thesis.

2. Theoretical Background

In this chapter, some basic theories of the noise equivalent power in fiber amplifiers will be first introduced. Then, the theory of two photon absorption and the absorption coefficient in semiconductors will be shown in the next.

2.1   Dual-Wavelength Amplification in Yb:Fiber Amplifier

Recently, fiber amplifiers working as an effective optical amplifier have been developed and applied in lots of amplifying systems. Fiber amplifiers are based on doped optical fibers as the gain media. Usually the core of the fiber is doped with different rare earth ions such as Erbium, Ytterbium, or Thulium. According to the different range of the wavelengths needed to be amplified, the rare earth ions with the gain peak at the input signal wavelength will be selected as the dopant. In my thesis, Ytterbium doped fiber (YDF) amplifiers are preferred as it produces high powers and a large gain bandwidth extending from 970nm to 1200nm, which allows us to separate the two colors over 60nm. Based on the YDF amplifiers, a dual-wavelength seed with peak wavelength around 1040nm and 1100nm will be amplified in the optical fibers.

The Figure 1 of R. Pachotta et. al. paper (Paschotta, 1997) shows the variation of the absorption and emission cross sections depending on wavelengths. Based on this figure, we use the 975nm diode laser as our pumping source due to the large absorption cross section around 975nm. The incident signal or the amplified wavelength region is around 1000nm to 1150nm, which includes our two required colors.

2.1.1   Light Amplification and Gain in Two-Level System

The fiber amplifier is based on the interaction between the light and the atoms. Atoms have levels which are separated by quantized energy levels. When the energy of the photon matches the energy difference of the two quantized energy levels, the atom can absorb the energy of a photon, and jump from the ground stage to the upper level. This process is called pump absorption. Similarly, the atom in the excited level can only stay in this level for a short period of time, known as the lifetime, and it will drop back down into a lower state, emitting a photon with an energy corresponding to the energy difference between the upper state and the lower state. This emission is known as spontaneous emission. However, if the atom is already in the excited state and other photons are present simultaneously, the atom can emit a photon exactly the same as the incident photons. This

kind of the emission is known as stimulated emission, and it is the basis of the fiber amplifier. An atom is excited from the ground state to the upper level by a laser, known as the pump, and then stimulated by another laser called the seed. The emission of the photons from the atoms add coherently to the incident seed laser, resulting in amplifying it along the fiber. The probability per unit time for absorption and stimulated emission can be written as

$$W = p_a = p_{st} = \eta \frac{c}{V} \sigma(\upsilon),\tag{1}$$

where V is the volume, c is the speed of light, η is the numbers of photons, and $\sigma(\upsilon)$ is the cross section of the transmission, which varied with wavelengths. The number of photons per unit time per unit area is also referred as the photon flux density, defined as

$$\phi = \frac{I}{h\upsilon},\tag{2}$$

where I is the intensity of the light. If the cross-sectional area of the fiber is A, the number of the total photons crossing this area in a second is

$$\eta = \phi A = \phi \frac{V}{c}.\tag{3}$$

Substitute this expression into Equation (1), the probability W can be rewritten as

$$W = \phi \sigma(\upsilon) = \frac{I}{h\upsilon} \sigma(\upsilon).\tag{4}$$

Once knowing the transition probability, one can easily determine the gain. Assuming that there are N_1 atoms staying in the lower energy level per unit volume, and then the average density of the absorbed photons is $N_1 W$. Similarly, if the upper energy level contains N_2 atoms per unit volume, the average density of photons created by stimulated emission is $N_2 W$. Assuming that the two-level system has a state of population inversion N, which means that $N = N_2 - N_1$ is positive, the gain on the photons density can be achieved. Along the propagation direction, z, the variation in the photon flux density per unit length can be written as

$$\frac{d\phi}{dz} = NW.\tag{5}$$

Then one can obtain the gain coefficient g as

$$g(\upsilon) = N\sigma(\upsilon). \tag{6}$$

The differential equation of the photon flux density can be established as

$$\frac{d\phi}{dz} = g(\upsilon)\phi(\upsilon). \tag{7}$$

Supposing that the original flux density is $\phi(0)$ at z=0, the flux density at certain position z in the fiber can be obtained as

$$\phi(z) = \phi(0)\exp[g(\upsilon)z]. \tag{8}$$

After the light propagates a distance L in the fiber, the gain can be written as

$$G(\upsilon) = \exp[g(\upsilon)L]. \tag{9}$$

From this above equation, it is obvious that the gain does not only depend of the length of the fiber, but also depend on the population of each energy level. In the simplest two energy level system, the variation of the upper level population can be determined by using the rate equation, when considering all the transitions due to pump absorption, spontaneous and stimulated emission. The rate equation of the upper energy level can be shown to be the following (Silfvast, 2004):

$$\frac{dN_2}{dt} = R - N_2(\frac{1}{\tau_{sp}} + \frac{I}{h\upsilon}\sigma_{se}), \tag{10}$$

where I is the incident intensity, R is the pumping flux, σ_{se} is the stimulated emission absorption, and τ_{sp} is the spontaneous lifetime of the upper energy level. For the above rate equation, we assume that the light beam is uniformly distributed in the core area of the fiber. Thus the gain and the intensity do not depend on the radius of the cross-sectional area of the fiber. However, the Equation (9) does show that the gain depends on the wavelength of the light and the propagation length in the fiber. In Equation 10, the first term on the right side of the equation represents absorption. The second and the third terms correspond to the spontaneous decay and stimulated emission from the upper level. In steady-state equilibrium, Equation 10 equals zero, since the steady state implies that there are no net changes in N_2, and the steady-state solution is

$$N_2 = \frac{R}{\dfrac{1}{\tau_{sp}} + \dfrac{I}{h\upsilon}\sigma_{se}} . \tag{11}$$

When $I = 0$, the maximum value of the population density is given as $N_2 = R\tau_{sp}$. As the incident beam with intensity I traverses a long gain medium, the intensity I increases due to the stimulated emission from the upper energy level. The intensity eventually becomes as large as the term associated with the level lifetime and it is defined as the saturation intensity I_{sat}. When saturation occurs, the population density N_2 decreases by a factor of 2. Moreover, any further increase in I will further decrease the population density of the upper level and so further decrease the gain in the medium. The defined saturation intensity here is that intensity at which the stimulated emission rate downward equals the upper level radiation decay rate:

$$\frac{I_{sat}}{h\upsilon}\sigma_{se} = \frac{1}{\tau_{sp}} . \tag{12}$$

The saturation intensity can be obtained from the above equation and written as

$$I_{sat} = \frac{h\upsilon}{\tau_{sp}\sigma_{se}} . \tag{13}$$

2.1.2   Amplification in Yb:Fiber and Noise Equivalent Power

The above treatment applies for an ideal two level system in which no two energy level degenerate. As referred to Ytterbium doped fiber amplifier, the treatment must be reconsidered for its degenerated energy levels. For ytterbium ion Yb^{3+} in the silica fiber, there are two energy bands- the $^2F_{7/2}$ ground or lower state manifold and the $^2F_{5/2}$ excited or upper state manifold in the wavelength region from 900nm to 1200nm. Among the excited manifold, there are three separated sublevels. Those three levels allow the doped ytterbium ions can absorb energy at a variety of wavelengths ranging from 850nm to 1070nm. In my thesis, we use the diode laser with center wavelength at 975nm. Thus we just focus our discussion on that pumping transition. The ground manifold contains four sublevels, which accept stimulated emission photons with wavelength from 1035nm to 1140nm. This more than 100nm separation allows us to obtain the 1038nm and the 1108nm stimulated emission pulses after the pumping fiber. The detailed structure of the two manifolds of the ytterbium ion is shown in Figure 2-1.
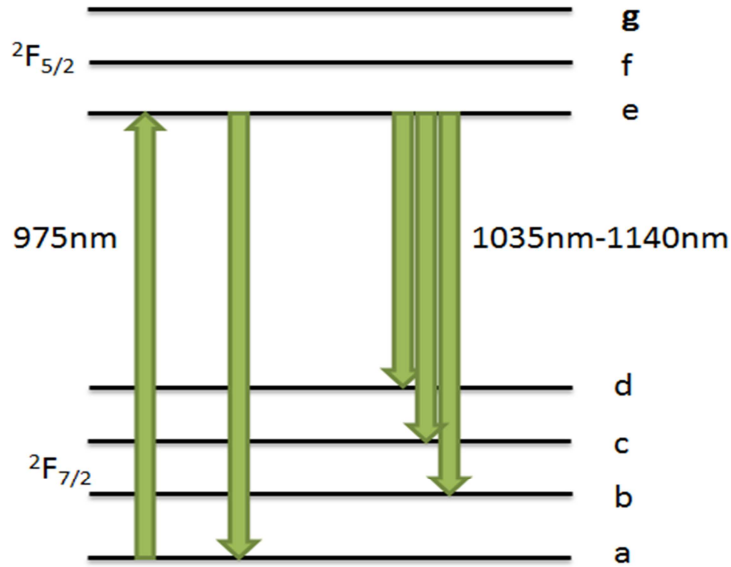
Figure 2-1 The two manifolds structure of the ytterbium ions. The possible transitions are indicated by wavelengths.

In Figure 2-1, due to the large of the band-gap between two manifolds, the multi-photon non-radiative decay rate is negligible. Thus all the absorption and the emission transitions will be included in two sublevels in each of the two manifolds. As mentioned before, the ions in the energy level a will be pumped into the excited state e by the 975nm diode laser. With the presence of our two colors with wavelength centered at 1038nm and 1103nm respectively, the excited ions quickly decay to levels b, c, and d, resulting stimulated emission photons to the incident seed photons. Finally, under fast thermalization, the ions in the sublevels b, c, and d will rapidly relax to the energy level a. Because of that fast thermalization, the population equations of the ytterbium ions can be regarded as a two-level energy scheme. Thus, the rate equation describing the two-level system can be used here for ytterbium doped fiber amplifier.

Back to the rate equation, the intensity I is the confined power in the fiber core per unit cross-sectional area. Suppose that the confined power is ΓP, where Γ the confinement factor for power P. The equation can be rewritten as

$$\frac{dN_2}{dt} = R - N_2 \left(\frac{1}{\tau_{sp}} + \frac{\Gamma P \lambda}{Ahc} \sigma_{se} \right). \tag{14}$$

Under the assumption that the gain spectrum of the ytterbium ions is homogenous, gain competition exists between the two colors and the ASE. The induced ASE can deplete the upper-level ions,

resulting in decreased gain for the two colors and a large ASE output after the fiber amplifier. In order to amplify the seed efficiently in the amplifier stages, the incident power of the seed has to be strong enough to compete with the induced ASE in the gain medium and extract enough gain. This is the reason why we will apply the theory of noise equivalent power to calculate the required incident power of the seed.

As referred to the ASE in the fiber, it is primarily generated from the spontaneous photons, which are the spontaneous emission noise in the fiber. In the pumped fiber, the stimulated emission process amplifies these initial photons and this process continues, resulting in a strong ASE at the output of the doped Yb:fiber. Assuming that the ASE is generated from one spontaneous photon from the same end with the incident seed, the minimum required power of the two colors can be obtained. From Equation 6, we can see that the gain is different at the different wavelengths. If we just consider one single wavelength, the initial spontaneous photon at the wavelength corresponding to the gain peak will be amplified and generate the ASE. The saturation power of the ASE can be obtained from Equation 13 as

$$P_{sat-ASE} = \frac{Ahc}{\Gamma \tau_{sp} \lambda \sigma_{se-ASE}}, \tag{15}$$

where A is the fiber cross area, λ is the wavelength of the ASE, and σ_{se-ASE} is the cross section for the ASE. Then the ASE generated by a single pass in the fiber can be written as

$$P_{sat-ASE} = P_{0-ASE} e^{g(\upsilon)z} = \frac{hc^2}{\lambda L} e^{g(\upsilon)z}, \tag{16}$$

where L is the length of the fiber and z is the saturation length. From Equation 16, we can easily get the saturation length of the ASE. However, the gain at the seed is smaller and the incident power of the seed needs to be sufficiently high to reach their saturation power in less length than the ASE saturation length. Thus, by applying the same z obtained from Equation 16, the required power of the seed can be written as

$$P_{0-Seed} = \frac{P_{sat-Seed}}{e^{g(\upsilon)z}}. \tag{17}$$

Based on the above noise equivalent power theory, some assumptions are made to simplify the calculation. Firstly, only the two peak wavelengths of the seed at 1038nm and 1103nm are

considered here for calculation. Secondly, all the atoms are pumped into the upper energy level and the population density in the lower energy level is zero. Thus $N = N_2 = N_{total}$. Finally, the gain coefficient is considered to be a constant as the small signal gain coefficient, which is shown as

$$g_{ss} = N_{total}\sigma_{se}(\upsilon).$$ (18)

In my calculation, I applied the same simulation results from Table 2.1 in Hajialamdari's thesis (Hajialamdari, 2013). The total population density of the Yb:fiber is $8\times10^{25}\,m^{-3}$. The confinement factors of the single-clad fiber and the double-clad fiber are both 0.83. The diameter of the single-clad fiber is 4μm, and the diameter of the double-clad is 6μm. However, the cross-section $\sigma_{se}(\upsilon)$ is not shown directly in his work. From the Figure 3.16 in Hajialamdari's thesis (Hajialamdari, 2013), we can assume the blue line represents the variation of the cross-section with different wavelength in a 7.5m-long pre-amplifier. In order to simplify the final results, I further assume the maximum cross-section at wavelength 1070nm is $10^{-25}\,m^{-2}$. Thus, my calculated saturation length of the ASE in this pre-amplifier is 2.785m, and the required powers of the blue color and the red color coupled in the fiber are 94μW and 1.69mW respectively. By applying the same method, we pick up the Figure 3.21 (b) in his thesis (Hajialamdari, 2013) as the emission cross section for the second and the third amplifier stage. For the second amplifier stage, the line representing the forward ASE in 8m double-clad Yb:fiber shows the variation of the cross section with different wavelength in counter-direction pump scheme. The calculated required powers for 1038nm and 1103nm are 2.86mW and 2.69mW respectively. The line for the ASE in 15m double-clad Yb:fiber is applied for the third amplifier stage calculation. The minimum required power of the blue color coupled in the fiber is 12.47mW, and that of the red color coupled in the fiber is 18.82mW.

The simulation results of the emission cross section show that the $\sigma_{se}(\upsilon)$ does not only depend on the wavelength, but also depend on the different kinds of fiber, different fiber lengths, different pump power, and different pumping schemes. Thus, the calculated results can be different for different amplifier stages. However, all the rough calculation results from the noise equivalent power theory can still give us the approximate required power of the seed for the each amplifier stage in our whole system. In addition, based on these results, the fiber length and the pump scheme can be decided.

2.2 Two Photon Absorption in Semiconductors

The phenomenon of two photon absorption (TPA) was first experimentally demonstrated in a europium doped crystal in 1961 (Kaiser, 1961). TPA arises from the imaginary part of the third-order nonlinear susceptibility (Boyd, 2008). Because of the large third-order nonlinearities in semiconductors (Fishman, 2011), TPA is particularly strong in semiconductors. In my thesis, we focus our interest on TPA in GaAs. Because of its crystal inversion symmetry, the lowest-order non-linearity in GaAs originates from the third-order optical susceptibility. In the presence of an input signal or two input signals, the third order nonlinear polarization P related to the TPA can be described respectively as (Dumon, 2006):

$$P^{(3)} = \varepsilon_0 \frac{3}{4} \chi^{(3)}(\omega; \omega, \omega, -\omega) |E_\omega|^2 E_\omega \tag{19}$$

$$P^{(3)} = \varepsilon_0 \frac{3}{2} \chi^{(3)}(\omega_2; \omega_1, \omega_2, -\omega_1) |E_{\omega_1}|^2 E_{\omega_2}, \tag{20}$$

where ε_0 is the permittivity of free space, $\chi^{(3)}$ is the third-order susceptibility, and E_ω is the electronic vector of the incident wave at wavelength ω. Equation 19 describes the degenerate TPA, while Equation 20 describes the non-generate TPA. As mentioned before, the absorption coefficient of the TPA is the related to the imaginary part of the $\chi^{(3)}$, and it can be represented as

$$\beta(\omega) = \frac{3\pi}{c\varepsilon_0 \lambda n_o^2} \text{Im}[\chi^{(3)}]. \tag{21}$$

In semiconductors, the TPA process will couple two photons when the total energy of the two input photons is greater than the band-gap energy of the semiconductors, and excites an electron from the valance band in to the conduction band, resulting in free carrier pairs. This can be illustrated in Figure 2-2.
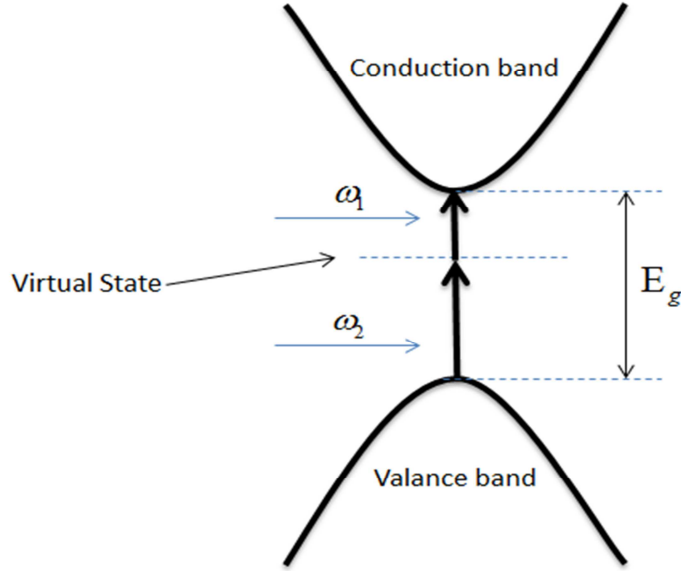
Figure 2-2 TPA in semiconductors.

According to the two incident photons, TPA can be categorized as degenerate TPA (D-TPA), non-degenerate TPA (ND-TPA), and extreme non-degenerate TPA (END-TPA). Two identical photons incident is the degenerate TPA, while two photons with different energies is the non-degenerate TPA. When the energy difference of the photons is very large, this kind of TPA is referred as END-TPA. In this situation, one of the photons has the energy very close to the band-gap energy of the semiconductor, while another one's energy is very small compared with the band-gap energy.

In order to measure the strength of the TPA, the two-photon absorption coefficient β in semiconductors has been studied both experimentally and theoretically. The transition rate for TPA per unit volume can be written as

$$W_2 = \frac{\beta I^2}{\hbar \omega},$$ (22)

where I is the intensity of the incident light. The transition rate of the TPA can be easily obtained by using the second order perturbation theory from the quantum mechanics view.

In this section, I will first discuss the derivation of the transition rate for the TPA. Then the transition rates will be simplified by using some assumptions on the band structure of the semiconductors both

for D-TPA and ND-TPA. At the end of this section, the basic theory of the sensitive MIR detector based on END-TPA will be introduced.

2.2.1 Two Photon Absorption Coefficient in Semiconductors

In this section, I will follow the quantum mechanics method to calculate the single and the two photon absorption rates used by Boyd (Boyd, 2008). The second-order perturbation theory is applied here for obtaining the transition rate for both D-TPA and ND-TPA.

From a quantum mechanics view, the atomic wave function $\varphi(\mathrm{r}, \mathrm{t})$ obeys the time-dependent Schrodinger equation

$$i\hbar \frac{\delta \varphi(\mathrm{r}, \mathrm{t})}{\delta t} = \hat{H} \varphi(\mathrm{r}, \mathrm{t}) \,, \tag{23}$$

where the Hamiltonian $\hat{H}$ is represented as

$$\hat{H} = \hat{H}_0 + \hat{V}(\mathrm{t}) \,. \tag{24}$$

In the above equation, $\hat{H}_0$ is the Hamiltonian for a free atom and $\hat{V}(\mathrm{t})$ is referred as the radiation interaction Hamiltonian, and it can be written as

$$H_{\mathrm{int}} = \hat{V}(\mathrm{t}) = -\hat{\mu} \tilde{E}(\mathrm{t}) \,, \tag{25}$$

where $\hat{\mu} = -e\hat{r}$. Assuming that the incident wave is monochromatic, we can simply write the field as

$$\tilde{E}(\mathrm{t}) = \mathrm{E} \mathrm{e}^{-i\omega t} + c.c. \,. \tag{26}$$

Without the incident interacting field, the wave functions associated with the energy eigenstates can be represented as

$$\varphi_n(\mathrm{r}, \mathrm{t}) = \mathrm{u}_n(\mathrm{r}) \mathrm{e}^{-i\omega_n t} \,, \tag{27}$$

where n is the energy level, and $\omega_n = E_n / \hbar$. $\mathrm{u}_n(\mathrm{r})$ is the coefficient and satisfies the eigenvalue equation without the interaction Hamiltonian

$$\hat{H}_0 \mathrm{u}_n(\mathrm{r}) = E_n \mathrm{u}_n(\mathrm{r}) \,. \tag{28}$$

With the presence of the interaction Hamiltonian, the general time-dependent Schrodinger equation can be written as

$$i\hbar\frac{\partial\varphi(\mathrm{r,t})}{\partial t}=(\hat{H}_0+\hat{V}(\mathrm{t}))\varphi(\mathrm{r,t})\,. \tag{29}$$

Because of the complete set of the energy eigenstates of the free atom Hamiltonian, the solution of the wave function can be expressed as a linear combination of those eigenstates

$$\varphi(\mathrm{r,t})=\sum_l a_l(\mathrm{t})\,\mathrm{u}_l(\mathrm{r})\,\mathrm{e}^{-i\omega_l t}\,, \tag{30}$$

where $a_l(\mathrm{t})$ gives the probability amplitude that, to the Nth order in the perturbation, the atom is in energy eigenstate l at time t.

Combined the Equation (29) and the Equation (30), we find

$$i\hbar\sum_l\frac{da_l}{dt}u_l(\mathrm{r})\mathrm{e}^{-i\omega_l t}+i\hbar\sum_l(-\mathrm{i}\,\omega_l)\mathrm{a}_l(\mathrm{t})\mathrm{e}^{-i\omega_l t}$$

$$=\sum_l\mathrm{a}_l(\mathrm{t})\,\mathrm{E}_l\mathrm{u}_l\mathrm{e}^{-i\omega_l t}+\sum_l\mathrm{a}_l(\mathrm{t})\,\hat{\mathrm{V}}\mathrm{u}_l\mathrm{e}^{-i\omega_l t}\,. \tag{31}$$

Based on the orthonormality condition of the eigenstates of the free atom Hamiltonian, we multiply both sides by $u_m^*(\mathrm{r})$ and integrate over all space, then we obtain

$$i\hbar\frac{da_m}{dt}=\sum_l a_l(\mathrm{t})\,\mathrm{V}_{ml}\,e^{-i\omega_{lm}t}\,, \tag{32}$$

where $\omega_{lm}=\omega_l-\omega_m$ and where $V_{ml}=\int u_m^*(\mathrm{r})\,\hat{\mathrm{V}}\mathrm{u}_l(\mathrm{r})d^3r$ are the matrix elements of the interaction Hamiltonian $\hat{\mathrm{V}}$.

Then we use the perturbation theory to expand the $a_m(\mathrm{t})$ in powers with the expansion parameter λ, which is assumed to vary continuously between zero and one

$$a_m(\mathrm{t})=a_m^0(\mathrm{t})+\lambda a_m^1(\mathrm{t})+\lambda^2 a_m^2(\mathrm{t})+\cdots. \tag{33}$$

By replacing the V_{ml} by λV_{ml} and equating powers of the λ on each side of Equation (32), we can obtain the set of equations

18

$$\frac{da_m^{(N)}}{dt} = \frac{1}{i\hbar} \sum_l a_l^{(N-1)} V_{ml} e^{-i\omega_{lm}t}, \quad N = 1, 2, 3 \cdots. \tag{34}$$

Before we derive the transition rate for the TPA, we need to find transition rate for linear absorption. We set N=1 for the first order interaction in the field. Without the present of the applied field, all the atoms are in the ground state and the other stages are empty for all times. Based on the previous equations, the interaction Hamiltonian matrix element can be represented as

$$V_{mg} = -\mu_{mg}(\mathrm{E}e^{-i\omega t} + \mathrm{E}^* e^{i\omega t}). \tag{35}$$

Substituting the above equations into equation, we can obtain

$$\frac{da_m^{(1)}}{dt} = \frac{1}{i\hbar} \mu_{mg}[\mathrm{E}e^{-i(\omega_{mg}-\omega)t} + \mathrm{E}^* e^{i(\omega_{mg}+\omega)t}]. \tag{36}$$

Integrating both sizes of the above the equation, the first order coefficient amplitude can be obtained as

$$a_m^{(1)}(t) = \frac{\mu_{mg}E}{\hbar(\omega_{mg}-\omega)}[e^{i(\omega_{mg}-\omega)t} - 1] + \frac{\mu_{mg}E^*}{\hbar(\omega_{mg}+\omega)}[\mathrm{E}e^{i(\omega_{mg}+\omega)t} - 1]. \tag{37}$$

The first term in the above equation is corresponding to one photon absorption, while the second one represents the stimulated emission. Thus we can neglect the second term but only focus on the absorption process. Since $a_m^{(1)}(t)$ is the probability amplitude, the probability of the atom at stage m at time t is given by

$$p_m^{(1)}(t) = \left|a_m^{(1)}(t)\right|^2 = \frac{\left|\mu_{mg}E\right|^2}{\hbar^2} \frac{4\sin^2[(\omega_{mg}-\omega)t/2]}{(\omega_{mg}-\omega)^2}. \tag{38}$$

For a large t, the above equation is proportional to t times a Dirac delta function. Thus, the probability of an atom in the state m can be written as

$$p_m^{(1)}(t) = 2\pi \frac{\left|\mu_{mg}E\right|^2 t}{\hbar^2} \delta(\omega_{mg}-\omega). \tag{39}$$

It is obviously that the probability is proportional to the time, and we can define a transition rate for the linear absorption by

$$W_{mg}^{(1)} = \frac{p_m^{(1)}(t)}{t} = 2\pi \frac{\left|\mu_{mg}E\right|^2}{\hbar^2} \delta(\omega_{mg} - \omega) \,. \tag{40}$$

Based on the previous method and results, we use the same way to solve the transition rate of the two photon absorption. Firstly, let us just consider the D-TPA. Because we already obtained $a_m^{(1)}(t)$, we can use this result on the right hand of the equation to solve $a_n^{(2)}(t)$ with setting N=2. The interaction Hamiltonian can be written as

$$V_{nm} = -\mu_{nm}E e^{-i\omega t} \,. \tag{41}$$

Here we dropped the negative-frequency contribution to V_{nm} for that term does not lead to two-photon absorption. Then we can obtain the time derivation form the second order probability amplitude. By integrating that over time and dropping some terms, which are not related to two-photon absorption, we can obtain

$$a_n^{(2)}(t) = \sum_m \frac{\mu_{mg}\mu_{nm}E^2}{\hbar^2(\omega_{mg} - \omega)} \left[\frac{e^{i(\omega_{mg} - 2\omega)t} - 1}{\omega_{ng} - 2\omega}\right]. \tag{42}$$

Thus the defined transition rate of D-TPA can be represented as

$$W_{ng}^{(2)} = 2\pi \left|\sum_m \frac{\mu_{mg}\mu_{nm}E^2}{\hbar^2(\omega_{mg} - \omega)}\right|^2 \delta(\omega_{ng} - 2\omega) \,. \tag{43}$$

Based on the same method and derivation steps, the transition rate of ND-TPA with ω_1 and ω_2 can be obtained

$$W_{ng}^{(2)} = 2\pi \left|\sum_m (\frac{\mu_{mg}\mu_{nm}E_1 E_2}{\hbar^2(\omega_{mg} - \omega_1)} + \frac{\mu_{mg}\mu_{nm}E_1 E_2}{\hbar^2(\omega_{mg} - \omega_2)}\right|^2 \delta(\omega_{ng} - \omega_1 - \omega_2) \,, \tag{44}$$

where E_1 and E_2 are the field amplitude of the two incident waves.

2.2.2   Degenerate TPA and Non-degenerate TPA

The general transition rate equations for D-TPA and ND-TPA can be applied in semiconductors. Generally, the electrons in the valance band can be excited to an intermediate state within the band gap of the semiconductor by absorbing one photon. Then another incident photon is absorbed, and

the electron finally jumps into the conduction band resulting in free pairs. Thus, the m stage shown in the above equation can be conduction states, valance states, or intermediate states. By replacing ω with $E = \hbar\omega$ in equation, we can easily get another representation of the transition rate for the ND-TPA. It can be written as (Hutchings, 1992),

$$W_2^{ND} = \frac{2\pi}{\hbar} \sum_{v,c} \left| \sum_i \frac{\langle \varphi_c | \hat{H}_2 | \varphi_i \rangle \langle \varphi_i | \hat{H}_1 | \varphi_v \rangle}{E_{iv} - \hbar\omega_1} + \frac{\langle \varphi_c | \hat{H}_1 | \varphi_i \rangle \langle \varphi_i | \hat{H}_2 | \varphi_v \rangle}{E_{iv} - \hbar\omega_2} \right|^2 \delta(E_{cv} - \hbar\omega_1 - \hbar\omega_2), \quad (45)$$

where 1 and 2 designate the two different photons, and v, c, and i are the valance, conduction, and intermediate states, respectively. Here the interaction Hamiltonian can be represented as

$$H_j = -\frac{e}{m_0 c} \tilde{E}_j \bullet \hat{\mu}, \quad (46)$$

where j is equal to 1 or 2, m_0 is the free electron mess.

In order to determine the transition rate for ND-TPA, we apply the simplest model for a semiconductor, which consists of a single parabolic conduction band and a single parabolic valance band in which the intermediate states are also these two bands (Hutchings, 1992). Thus the transition rate can be simplified as

$$W_2^{ND} = \frac{2\pi}{\hbar} \left| \frac{H_2^{cv} H_1^{vv}}{-\hbar\omega_1} + \frac{H_1^{cv} H_2^{vv}}{-\hbar\omega_2} + \frac{H_2^{cc} H_1^{cv}}{\hbar\omega_2} + \frac{H_1^{cc} H_2^{cv}}{\hbar\omega_1} \right|^2 \delta(E_{cv} - \hbar\omega_1 - \hbar\omega_2), \quad (47)$$

where H^{cv}, H^{vv}, and H^{cc} are all the interaction Hamiltonian matrix elements. E_{cv} is the energy difference between the conduction band and the valance band. In this equation, the wave functions are all in the space region. Because the band structure of the semiconductor is conventionally in the k space, we rewrite the above equation in k space as

$$W_2^{ND} = \frac{2\pi}{\hbar} \int \frac{d^3k}{(2\pi)^3} \left| \frac{H_2^{cv} H_1^{vv}}{-\hbar\omega_1} + \frac{H_1^{cv} H_2^{vv}}{-\hbar\omega_2} + \frac{H_2^{cc} H_1^{cv}}{\hbar\omega_2} + \frac{H_1^{cc} H_2^{cv}}{\hbar\omega_1} \right|^2 \delta(E_{cv} - \hbar\omega_1 - \hbar\omega_2). \quad (48)$$

Here $E_{cv}(\vec{k})$ depends on the k vector.

According to the statements of Wherrett (Wherrett, 1983), the inter-band transition matrix element can be represented as

21

$$\left\langle \varphi_c(\vec{k}) \middle| \hat{\mu} \middle| \varphi_v(\vec{k}) \right\rangle \approx \left\langle \varphi_c(0) \middle| \hat{\mu} \middle| \varphi_v(0) \right\rangle = \mu_{cv}. \tag{49}$$

This equation also shows that the inter-band-transition matrix element μ_{cv} is independent of k vector. By substituting this result into the inter-band-transition Hamiltonian matrix element H_j^{cv}, we can obtain

$$H_j^{cv} = -\frac{eE_j}{m_0 c}(\hat{\mu} \cdot \hat{a}) \delta(\mathrm{k}_c - \mathrm{k}_v), \tag{50}$$

where k_c and k_v are the k vectors for conduction band and valance band respectively, and $\hat{a}$ is the unit vector of the incident electric filed. Here, the delta function arises from the orthogenetic property of the wave functions. This term is nonzero only when $\mathrm{k}_c = \mathrm{k}_v$, which limits all the transitions between the two bands to be direct transitions. Wherrett also gave the representations for the matrix elements of the self-transitions

$$\left\langle \varphi_c(\vec{k}) \middle| \hat{\mu} \middle| \varphi_c(\vec{k}) \right\rangle = \frac{m_0 \hbar \vec{k}}{m_c} \tag{51}$$

$$\left\langle \varphi_v(\vec{k}) \middle| \hat{\mu} \middle| \varphi_v(\vec{k}) \right\rangle = \frac{m_0 \hbar \vec{k}}{m_v}, \tag{52}$$

where m_c and m_v are the masses of the electrons in the conduction band and the valance band, respectively. Based on those equations, the Hamiltonian matrix element can be written as

$$\mathrm{H}_j^{cc} = -\frac{eE_j}{m_c c} \hbar \vec{k}_c \cdot \hat{a} \tag{53}$$

$$H_j^{vv} = -\frac{eE_j}{m_v c} \hbar \vec{k}_v \cdot \hat{a}. \tag{54}$$

By substituting Equations (49), (52), and (53) into Equation (48), we can further simplify the transition rate of the ND-TPA as

$$W_2^{ND} = \frac{e^4 E_1^2 E_2^2}{4\pi^2 \hbar m_0^2 c^4} \int d^3 k (\hat{\mu} \cdot \hat{a})_{cv}^2 \cdot (\vec{k} \cdot \hat{a})^2 [-\frac{1}{\omega_1 m_v} - \frac{1}{\omega_2 m_v} + \frac{1}{\omega_2 m_c} + \frac{1}{\omega_1 m_c}] \delta(\mathrm{E}_{cv} - \hbar\omega_1 - \hbar\omega_2). \tag{55}$$

By applying the relationship $\dfrac{m_0}{m_c} = -\dfrac{m_0}{m_v} = \dfrac{2|\mu_{cv}|^2}{m_0 E_g}$ (Sheik-Bahae, 1991), the transition rate becomes

$$W_2^{ND} = \frac{2^5 I_1 I_2 e^4 \hbar^5}{n_1 n_2 E_g^5 c^2 m_c^2} \cdot \frac{1}{x_1^2 x_2^2} (\frac{1}{x_1} + \frac{1}{x_2})^2 \int d^3 k (\hat{\mu} \cdot \hat{a})_{cv}^2 \cdot (\vec{k} \cdot \hat{a})^2 \delta(E_{cv} - \hbar\omega_1 - \hbar\omega_2), \qquad (56)$$

where $x_1 = \dfrac{\hbar\omega_1}{E_g}$ and $x_2 = \dfrac{\hbar\omega_2}{E_g}$, n_1 and n_2 are the refractive indexes for wave 1 and 2, respectively.

Here, we also replace the E by the intensity of the light using $E_j^2 = \dfrac{8\pi c I_j}{n_j \omega_j^2}$.

As mentioned before, we use the simplest two parabolic bands for our band structure. The conduction band and the valance band can be represented as

$$E_c = E_g + \frac{\hbar^2 k^2}{2m_c}, \qquad (57)$$

$$E_v = -\frac{\hbar^2 k^2}{2m_v}. \qquad (58)$$

In the vicinity of the vertex of the parabolic shape valance band, $E_v \approx 0$. Thus, the energy difference between two bands is

$$E_{cv} = E_c - E_v = E_g + \frac{\hbar^2 k^2}{2m_c}. \qquad (59)$$

By integrating in the k space and considering the delta function, the transition rate can be written as

$$W_2^{ND} = \frac{2^7 \pi I_1 I_2 e^4}{n_1 n_2 E_g^4 c^2 m_c} \cdot A\sqrt{E_g} \sqrt{m_c} \cdot \frac{1}{x_1^2 x_2^2} (\frac{1}{x_1} + \frac{1}{x_2})^2 (x_1 + x_2 - 1)^{3/2}, \qquad (60)$$

where A is just a constant resulting from the angular dependent terms $(\hat{\mu} \cdot \hat{a})_{cv}^2$ and $(\vec{k} \cdot \hat{a})^2$ in the integral (Sheik-Bahae, 1991).

Rewrite the above equation, we can obtain

$$W_2^{ND} = K \frac{\sqrt{E_p}}{E_g^4} \frac{I_1 I_2}{n_1 n_2} F_2(\frac{\hbar\omega_1}{E_g}; \frac{\hbar\omega_2}{E_g}),$$ (61)

where $E_p = \frac{2|p_{cv}|^2}{m_0}$, $K = \frac{2^{14} A\pi e^4}{\sqrt{m_0} c^2}$, and $F_2^{ND}(x_1; x_2) = \frac{(x_1 + x_2 - 1)^{3/2}}{2^7 x_1^2 x_2^2}(\frac{1}{x_1} + \frac{1}{x_2})^2$. Here E_p is

nearly material independent and possesses a value of $E_p \simeq 21eV$ for most direct gap

semiconductors. However, K is a material-independent constant. In my derivation, the K value is little

different from that value obtained by Sheik-Bahae (Sheik-Bahae, 1991), for they used different

method under different assumptions to solve that. Compared with those two values, the only

difference is a constant number. That is why I add a factor A in the expression K for further correction.

$F_2^{ND}(x_1; x_2)$ just depends on the two incident photons and the band-gap energy of the

semiconductor.

Based on the expression of the transition rate, the absorption coefficient of the DN-TPA can be

obtained as

$$\beta_2^{ND}(\omega_1; \omega_2) = K \frac{\sqrt{E_g}}{n_1 n_2 E_g^3} F_2(\frac{\hbar\omega_1}{E_g}; \frac{\hbar\omega_2}{E_g}),$$ (62)

for $\beta_2^{ND}(\omega_1; \omega_2) = \frac{\hbar\omega_1 W_2^{ND}}{I_1 I_2}$.

Similarly, one can follow the same method to solve the coefficient of D-TPA

$$\beta_2^{D}(\omega) = K \frac{\sqrt{E_g}}{n_0 E_g^3} F_2(\frac{\hbar\omega}{E_g}),$$ (63)

where $F_2^D(x) = \frac{(2x-1)^{3/2}}{(2x)^5}$.

Comparing $F_2^D(x)$ with $F_2^{ND}(x_1; x_2)$, when the difference between x_1 and x_2 is large, $F_2^{ND}(x_1; x_2)$

can be 1000 times larger than $F_2^D(x)$. An ND-TPA and END-TPA enhancement of a factor of 100-

1000 over D-TPA in direct-bandgap semiconductors has been demonstrated theoretically. Based on

this large enhancement on absorption, the photons or the beam at MIR wavelength region can be

easily detected by the presence of another photon or beam with a different wavelength. Once the total photon energy of the two photons exceeds the band gap energy of the semiconductor, the photon-generated carrier density N can be given by

$$\frac{dN}{dt} = 2\,\mathrm{K}\,\frac{\sqrt{E_g}}{n_1 n_2 E_g^4} F_2(\frac{\hbar\omega_1}{E_g};\frac{\hbar\omega_2}{E_g})I_1 I_2\,.$$

(64)

In addition, TPA does not need the phase matching condition, making it a simpler experimental technique than parametric nonlinear processes

3. Experimental Setup and Procedures

In my thesis, in order to achieve more powerful MIR radiation with a larger spectral separation than what our group had already achieved, we developed a three-stage Yb:fiber CPA system with one single-clad Yb-doped-fiber pre-amplifier and two double-clad Yb-doped-fiber amplifiers. In my experimental setup, the pre-amplifier is pumped by a 975-nm laser diode with a maximum average power of 150mW in a counter-direction pumping scheme. However, one more Yb doped fiber amplifier was added in my new setup to achieve more intense dual-wavelength seeding to the final amplifier, resulting in a more efficient amplification in the final stage. The output after the three-stage Yb:fiber amplifier produces more powerful two colors with less ASE induced in amplifiers.

The fiber CPA technology is still applied here due to the fact that the ultra-short pulses with high intensity can easily produce unexpected nonlinear effects in the tight core area of the fiber. To avoid that, fiber CPA was employed which maximizes the average and the peak powers of the whole system.

Another point I have to mention here is our new method for detecting MIR radiation based on END-TPA in direct band-gap semiconductor GaAs. This novel detector of MIR radiation has been proved to have a better performance than conventional MCT detectors (Fishman, 2011). They also predicted that the larger difference between two incident photon frequencies, the more sensitive for this detector. We are trying to use 920nm (1.347eV) and 17.6μm (0.07eV) pulses to prove that prediction and develop a new MIR detector. Moreover, the pulse duration of the ultra-short MIR radiation cannot be measured in our previous experimental setup. By applying the END-TPA techniques, the pulse duration of MIR can be measured using this novel detective system.

The general schematic diagram of the experimental apparatus is shown in Figure 3-1. At the beginning, a 200fs laser oscillator centered at 1030nm was used as the source for dual wavelengths. A broadband width pulse was generated by focusing the output of the oscillator into a photonic crystal fiber (PCF). An extended spectral ranged from 900nm to 1150nm is obtained after the PCF. Next, a 100m-length single mode fiber was spliced to the PCF for stretching the pulse and a Faraday isolator was applied to protect the oscillator from the backward travelling pulses. After the isolator, the total power of the continuum decreased from 150mW just after the oscillator to 26mW. Then a pulse stretcher was used to select the two colors by eliminating 60nm spectrum between them. In addition, the two-color pulses were also stretched in the time domain. When pumped, the Yb doped

fiber produced ASE that could be really strong around the spectral gain peak. Thus the incident seed must be stronger than the power of the ASE in order to extract gain more efficiently. Since the dual wavelengths were still weak from the super-continuum generation, a pre-amplifier was necessary here to improve the power of the seed wavelengths before they were amplified in the main amplifiers. Then, two main amplifiers with different lengths of double-clad Yb doped fibers were employed to amplify the two colors. One interference filter was used between the amplifiers to eliminate the ASE from the second amplification stage. Before the second amplification stage, another Faraday isolator was placed to block the backward travelling radiation. The two colors were next compressed to near their original pulse durations. Finally, the two colors were incident onto a 1-mm GaSe crystal for MIR generation. Two experimental systems were set up for detecting the MIR radiation. One of them is conventional MCT detector, which is attached to a lock-in amplifier. In order to confirm the measured power of the MIR from the MCT detector, we also measured the MIR with a thermal power meter. The second method uses GaAs semiconductor to measure END-TPA. In our experiment, we combined the GaAs detector with a Lock-in amplifier, needed for more sensitive detection of the MIR radiation.
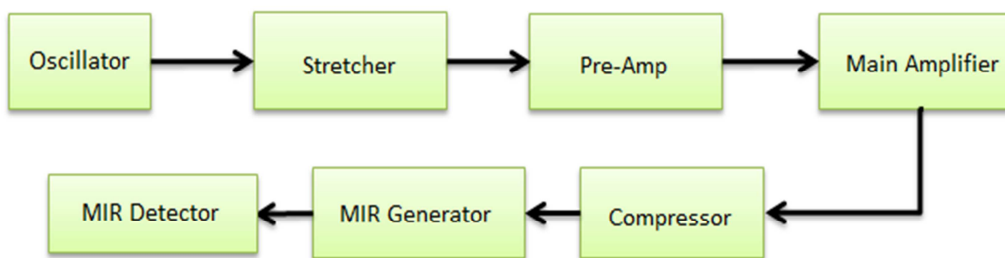

Figure 3-1 The general schematic diagram of the dual-wavelength Yb:fiber CPA.

3.1 Front-end Laser System

In this part of our system, I used the previous experimental setup (Al-Kadry, 2011). This front-end laser system for super continuum generation is shown in Figure 3-2.

The seed of the whole experiment is produced by a 150mW average power Yb:fiber oscillator centered at 1030nm. This laser oscillator can generate 200fs pulses at a repetition rate of 50MHz. In order to generate a continuum spectrum, the output beam of our oscillator is collimated by 10X microscope objective with a numerical aperture NA=0.25. Another identical microscope objective was used to couple the collimated beam into a 2-m PCF with a zero dispersion wavelength (ZDW) at

1040nm. In this coupling system, 50% of the incident power is estimated to be coupled into the PCF (Al-Kadry, 2011). The reason why we chose the PCF with ZDW at 1040nm is because this ZWD is very close to the peak wavelength (1030nm) of our launched pulses. When the incident wavelength is close to the ZDW of the nonlinear PCF, the ultra-short high intensity pulses will have a long interacting distance with the nonlinear medium before they are temporally broadened (Alfano, 2006). Using a PCF dramatically increases nonlinear effects and a super-continuum spectrum from 900nm to
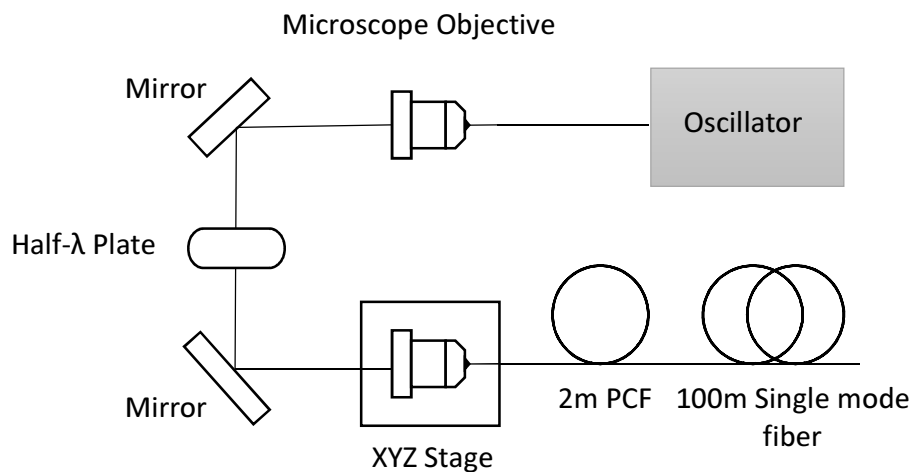

Figure 3-2 Experimental Setup for super continuum generation by using a femtosecond Yb:fiber oscillator and 2m PCF.

1150nm can be generated after just a 2m length of PCF.

A half-wave plate was placed before the 2-m PCF to rotate the polarization of the incident ultrafast pulses in order to generate different spectra. The output power is 26mW measured by our power meter. The loss of the power from 150mW to 26mW is mainly due to the poor coupling ratio into the PCF after the oscillator. Moreover, the reflecting mirrors and the Faraday isolator made contributions to the decrease in power.

Another important part of this front-end laser system is the 100m single-mode fiber. The purpose of this fiber is to stretch the short-wavelength color, for the short wavelength pulses experience negative dispersion in the amplifier and the grating stretcher could not sufficiently stretch the short wavelength pulses (Al-Kadry, 2011). It is known that a fiber in the normal dispersion regime can broaden the short pulses. The pulse broadening in the fiber can be written as (Yariv, 2006)

$$\Delta\tau = D\Delta\lambda L, \qquad (65)$$

28

where $\Delta\lambda$ is the wavelength bandwidth of the pulses, L is the propagation distance in the fiber, and D is the dispersion coefficient and is defined as

$$D = -\frac{\lambda}{c}\frac{d^2 n}{d\lambda^2}. \qquad (66)$$

The n in the above equation is the refractive index of the fiber and can be found in many references. For my calculation, the refractive index in the Yb:fiber can be described by following (Yariv, 2006)

$$n = 1.4508554 - 0.0031268\lambda^2 - 0.0000381\lambda^4 + \frac{0.0030270}{\lambda^2 - 0.035} - \frac{0.0000779}{(\lambda^2 - 0.035)^2} + \frac{0.0000018}{(\lambda^2 - 0.035)^3}. \qquad (67)$$

Because we only need to consider about the peak wavelengths of the two colors at 1038nm and 1103nm, the calculated pulse broadening for them are about 25ps and 19ps respectively.

3.2 Grating Stretcher

The purpose of applying this grating stretcher is twofold: further pulse stretching and selecting the two colors from the super continuum spectrum. Achieving a 60nm spectral separation between the two colors and stretching both colors with a pair of 20mm-wide transmission gratings used in this system was not possible. Thus, a three-grating system was used for our stretcher and it is depicted in Figure 3-3.
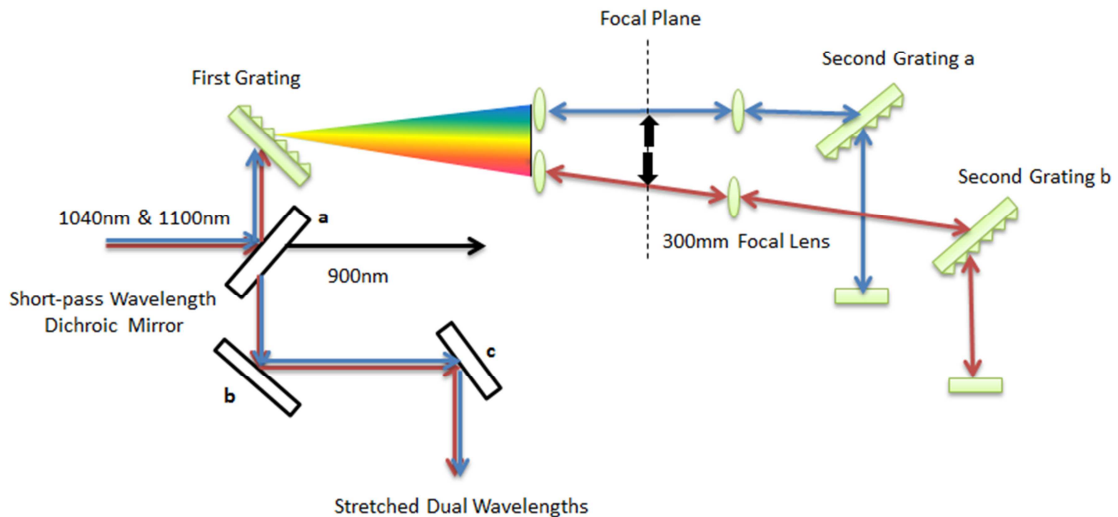

Figure 3-3 The schematic diagram of the grating stretcher.

As shown in this figure, this system is mainly comprised of three p-polarized 1250 lines/mm gratings from Ibson Photonics, and four 300mm-focal-length 2.5-cm-diameter focusing lenses forming two unity magnification telescopes. This combination of transmission gratings and internal lenses can be used to offer normal dispersion, which leads to pulse broadening. Two movable knife edges are placed in the focal planes of the focusing lenses for eliminating unwanted spectral components. It is also shown that two roof-type reflectors are applied here to double the path of the pulses passing through the gratings and output circular beams.

At the output of the fiber stretcher, a half-wave plate was rotated to change the polarization of the super-continuum pulses to match the p-polarized gratings for the maximum diffraction efficiency. After hitting the short-wavelength pass dichroic mirror in Figure 3-3, the spectrum with wavelengths longer than 1μm was reflected toward the first grating and the short wavelength spectrum transmitted through the dichroic to be used for END-TPA. The reflected beam hits the lower half of the first grating. For maximum diffracted power, a power meter was placed after the first grating to measure the minimum transmitted power. It can be achieved by rotating the grating and the maximum diffracted power is obtained at an angle of incident of 42 degrees, which is the angle between the normal line of the grating and the incident beam. After diffracting through the first grating, the spatially stretched spectrum travels toward the first two lenses located at 228.6mm away from the first grating. Those two lenses can be used to select two colors from the continuum. Then, two movable knife edges work as a perfect notch filter to select the two colors. When passing through another two lenses, the two colors will travel towards the last two gratings, the second grating a and the second grating b. Those two gratings were placed anti-parallel to the first grating. The distance between the second lens and the second grating, a for 1038nm is 45mm, while the distance between the second lens and the second grating, b for 1103nm is 182mm. After diffracting through the second gratings, both colors will be reflected back to the upper side of the second gratings by the roof-type reflectors made up by two perpendicular mirrors. The mirrors in the reflectors are adjusted to have the reflected beams return just above the incident beams. The paths of the incident beam and the reflected beam can be shown more clearly in Figure 3-4.
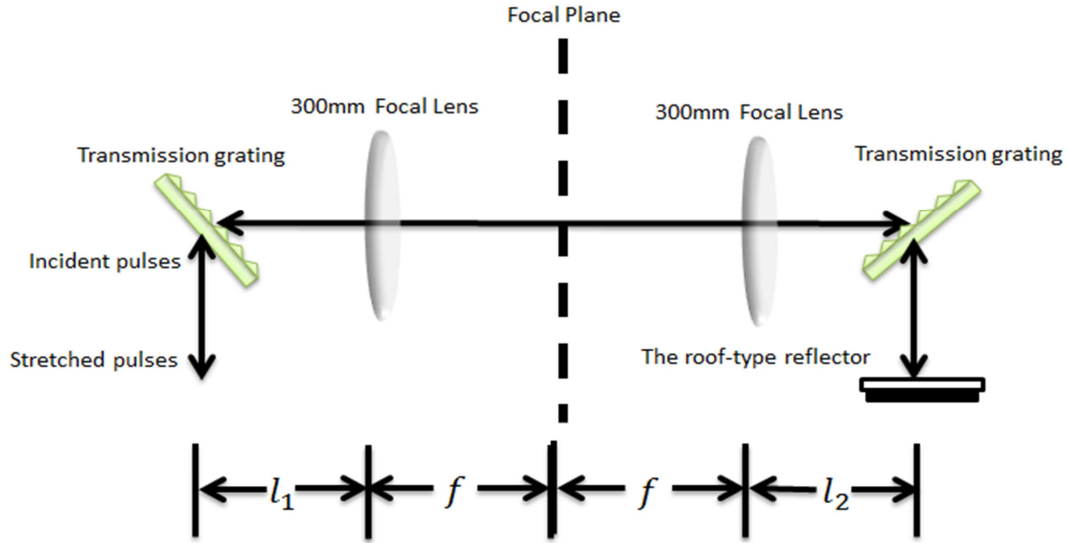
Figure 3-4 The top view of the grating pairs with internal lenses.

One of the most important purposes of this setup is to stretch the dual wavelengths. The pulse broadening can be calculated according to the setup. In Figure 3-4, l_1 and l_2 are the distance between the first grating and the first focal lens and the distance between the second grating and the second focal lens respectively. The focal lengths f of the two lenses are the same. The produced group delay dispersion (GDD) or the second derivative of the phase function can be represented as (Martinez, 1987)

$$GDD = \frac{d^2\phi}{d\omega^2} = \frac{\lambda^3(2f - l_1 - l_2)}{2\pi c^2 d^2 \cos^2\theta_D},$$

(68)

where the λ is the wavelength of the incident light, c is the light speed in vacuum, d is the grating period, and the θ_D is the diffraction angle. According to this equation, we can easily calculate the GDD of the two colors of 1038nm and for 1103nm respectively. Based on those results, the pulse broadening after propagating in a dispersive system is approximated shown by (Diels, 2006)

$$\Delta\tau = GDD\Delta\omega.$$

(69)

Thus the pulse broadening for 1038nm is about 49ps and for 1103nm is about 30ps.

After the stretcher, the two colors are sent to mirror b. After the stretcher, there can be a spatial chirp on the two-color beam because the gratings are not perfectly anti-parallel. The spatial chirp can

be measured by sending the two colors into the spectrometer which is coupled to a single-mode fiber at the input. By adjusting the knobs of the second grating a and second grating b, the spatial chirp can be minimized until the observed spectrum decreases and increases uniformly when scanning the incident beam at the input to the spectrometer to the left and right.

3.3   Pre-amplifier

Due to the weak output of the two colors from the super continuum generation, it is necessary to set up a pre-amplifier for the two colors. The two-color output of the pre-amplifier will have sufficient power to compete with the ASE in the next amplifiers. In the previous work mentioned in Chapter 1, a double-end pumped fiber pre-amplifier had been built. Because one of the pump laser diodes used in the previous work died, we had to change the double-end pumping scheme into a single pump system. In my thesis, the pre-amplifier still contains a single-clad, single-mode Yb:fiber but pumped by only one 150mW laser diode centred at 975nm in a counter-direction pumping scheme. The optimized fiber length has been obtained by Hajialamdari (Hajialamdari M. A., 2011). According to his simulation, the optimizing length for the pre-amplifier is 7.5m. The more detailed experimental setup is shown in Figure 3-5.
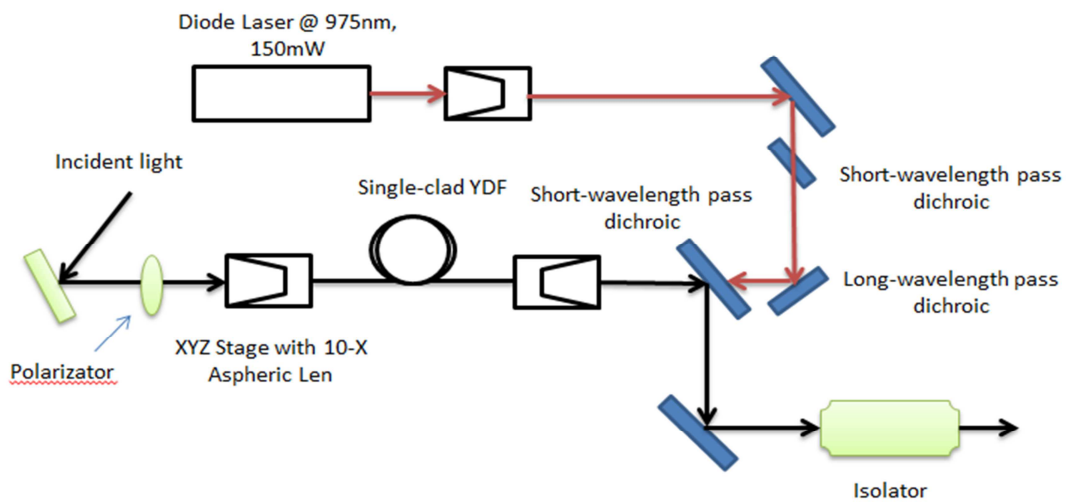

Figure 3-5 Experimental Setup of the pre-amplifier system.

In this pre-amplifier system, the collimated two-color beam was sent into a 7.5m low-doped, single-mode, and single-clad Yb:fiber. In order to avoid the fiber lasing on its own, the Yb:fiber was angle cleaved at 8 degrees at both ends. On the incident side, the two-color seed was focused into the Yb:fiber by an anti-reflection-coated (AR-coated) aspheric lens. On the output side, another AR-

coated aspheric lens was used. For the collimation of the output beam from the pumping laser diode, another AR-coated aspheric lens was used. At the output, a short-wavelength pass dichroic mirror was used to reflect the two colors to the next amplifier stage. A long-wavelength pass dichroic mirror was to reflect the pumping beam into the pre-amplifier fiber. Those two dichroic mirrors allowed the short wavelength pump beam and the seed beam to share the same optical path and allowed the short wavelength pump beam to be focused into the output side of the pre-amplifier fiber. In addition, the dichroic mirrors protect the pump laser diode from the output of the pre-amplifier. For further protection, another short-wavelength pass dichroic mirror was placed closer to the output end of the laser diode. After the pre-amplifier fiber, a Faraday isolator was applied to protect the pre-amplifier and the oscillator from the backwards radiation from the amplifiers.

In the shorter-wavelength side of 1070nm, the Yb:fiber has a quasi-three level behavior. Thus the seed signal centered at 1038nm exhibits a strong absorption when propagating in an unpumped Yb:fiber. In contrast, the absorption of a seed pulse centered at 1103nm is very weak. Thus, the alignment of the long wavelength through the core of the Yb doped fiber can be easily accomplished without the pump. A power meter can be placed on the other side of the fiber to measure the output power. By tweaking two mirrors at the incident side of the fiber, the long wavelength beam could be coupled into the core of the fiber with efficiency around 50%. For the coupling of the seeding at wavelength around 1038nm, the re-absorption is very high and it can hardly propagate though the fiber to the other end. Under this situation, the pump was first coupled into the single mode fiber. The same method was used here. The power meter was placed at the other end of the fiber, and the pump beam can be coupled into the fiber by adjusting the reflecting mirrors. Then with the help of the pump, even tiny coupled power from 1038nm beam can be measured by the power meter at the output of the pre-amplifier. The coupling efficiency of the short-wavelength seeding can be improved by tweaking the back mirror or the reflectors after second grating b. By adjusting the back mirror and the front two mirrors at the incident side of the pre-amplifier several times, two colors can coincide with each other and both be coupled into the single-mode fiber. Because the Yb doped fiber in the pre-amplifier stage is a non-polarization preserving fiber, the polarizations of the two colors were different after the pre-amplifier. A half-wave plate was placed at the incident end of the pre-amplifier for changing the power ratio of the two colors after the Faraday isolator at the output.

3.4   Two Main Amplifiers

In our previous work, only one stage amplifier was used as the main amplifier. However, the 500mW single-mode pump laser diode died. The pre-amplifier with only one pumping diode is not sufficient to amplify the two colors to a high enough power level for the next amplifier stage. Thus we have developed a more complicated main amplifier system with two amplification stages. Moreover, the three-stage amplifier system is better, because it can amplify the seed and supress the ASE more efficiently. Both of the two stages used single-mode, highly-doped, and double-clad Yb:fibers in a counter direction pumping scheme. Two stages were setup by using two different lengths of the Yb:fiber, optimized for the best balance between the two colors after the whole amplifying system.

In the pre-amplifier, the single-mode single-clad Yb:fiber was used as the gain medium. Because of the tight core area (4μm fiber core), only the fundamental mode can propagate in the single-mode single-clad fiber. This limits the pump laser diode to a single-mode pump laser diode. Compared with
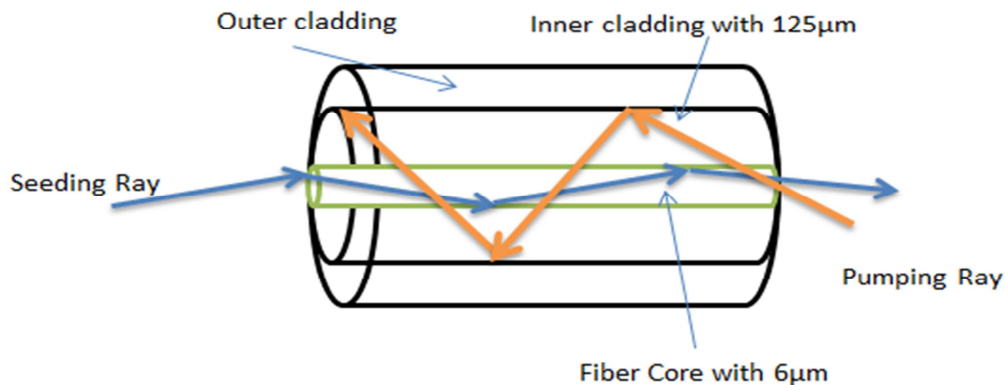

Figure 3-6 Schematic diagram of the double-clad fiber.

the single-clad fiber, the fibers used in our main amplifiers were double-clad. This kind of fiber has one 6μm diameter single-mode fiber core, one 125μm diameter inner cladding and one outer cladding. The inner cladding can accommodate higher modes propagating though the fiber. This is depicted in Figure 3-6. The pump ray will be coupled into the inner cladding with a zig-zag path. For each time the pump ray passes through the fiber core, the doped ions in the fiber core will be pumped. The double-clad Yb:fiber allows us to use more powerful multi-mode lasers to pump it, resulting in a more powerful output after this amplifier.

To optimize the seed coupling into the single-mode core of the double-clad fibers, an optical fast diode combined with an oscilloscope is used. Because the Yb doped fiber is almost transparent for the long-wavelength color, the beam at 1103nm was first coupled into the fiber. To accomplish this, the two mirrors in front of the input end were tweaked to maximize the observed power by the power meter placed at the output end of the fiber. However, this does not mean that the seeding has been coupled into the fiber core. Then we need to couple the pumping beam into the fiber by using the same method. After that, the fast diode connected to an oscilloscope was used to measure the backward ASE output power of the pumped fiber. Maximizing the ASE corresponds to the optimal coupling of the pump, the one that ensures the maximum absorption of the pump through the core of the fiber. With the pump and the seed, the fast diode was placed at the output of the amplifying fiber to measure the amplified signal. At the beginning, the pump driver was set at some certain pump current without the seed incident. The ASE in the fiber is shown as a DC voltage level measured by the oscilloscope. When the seed was sent into the fiber, the amplified pulses were observed by the oscilloscope corresponding to the gain extracted by the seed. The coupling of the seed was optimized by tweaking the two mirrors while observing the amplitude of pulses presented on the oscilloscope.

The experimental setup for the second amplifier is shown in Figure 3-8. The two-color output from the pre-amplifier is first sent to a telescope for up-collimating the beam size. The telescope includes two lenses with focal length 10cm and 25cm respectively. The second lens was located on a translation stage used to vary the numerical aperture for optimizing coupling. At the input end of the amplifier system, an AR-coated aspheric lens with numerical aperture (NA) 0.4 was used for coupling the seed beam into the fiber core. Another two AR-coated lenses with NA 0.25 were used on the output end of the amplifier fiber and the fiber output of the pump laser diode. The pump laser diode here was a multi-mode laser diode centered at 975nm with a maximum average power of 6W. Two long-wavelength pass dichroic mirrors were used to protect the pump laser diode. A short-wavelength pass dichroic mirror reflected the amplified two colors to the next stage. A notch filter was placed after the output end of the Yb:fiber to remove the produced ASE spectrum between the two colors. After that, two colors were sent to a half-wave plate and a Faraday Isolator by a large-bandwidth high reflector. The isolator is used to protect the oscillator and the previous amplification stage from any returning signal, and the half-wave plate is used to change the transmission of the two-color output when travelling through the polarized isolator.
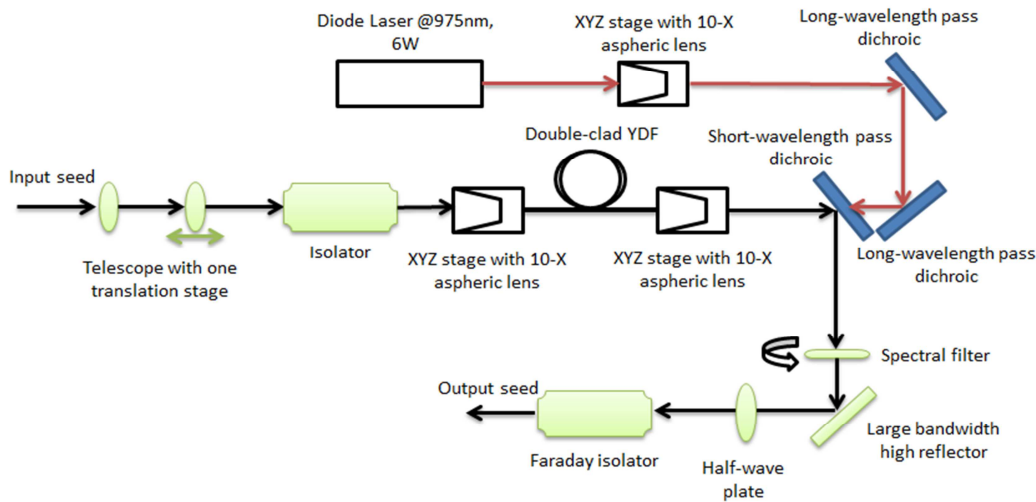
Figure 3-8 The Schematic diagram of the second amplifier with 5m double-clad Yb:fiber.

In my thesis, another trial experimental setup has been developed by us to amplify the two colors. Figure 3-7 shows the detailed experimental setup of this second amplification stage. A 5-m-length single- mode, single-clad, and highly doped Yb:fiber was pumped by a single-mode laser diode with central wavelength at 975nm. The pump beam was coupled into the fiber at the same of end with the incident two colors. The two long-wavelength pass dichroic mirrors were used to protect the pump laser diode. The Faraday isolator in front of the incident end of the Yb:fiber was used to protect the oscillator and the pre-amplifier. At the other end of the Yb:fiber, two notch filters placed on rotational stages were applied to block the unwanted ASE induced from the pumped single mode Yb:fiber.
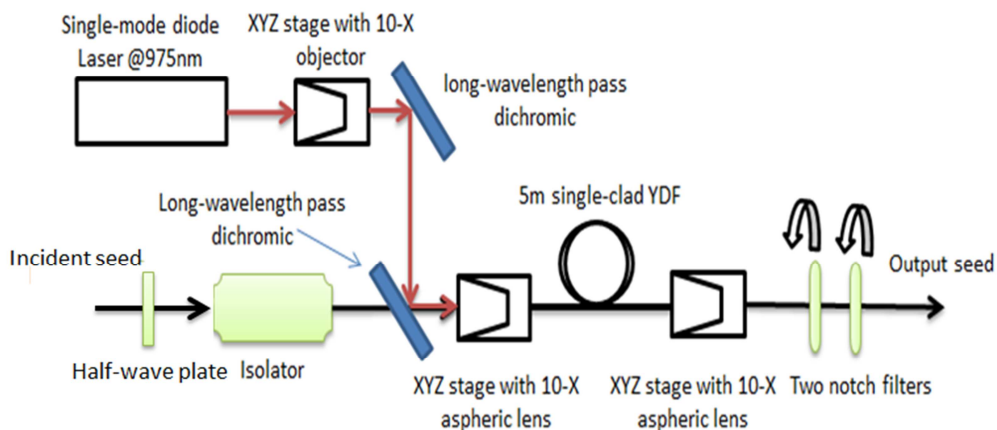

Figure 3-7 The schematic diagram of the second amplifier stage with 5m single mode Yb:fiber.

The similar setup for the third amplification stage is shown in Figure 3-9. In this amplification stage, a 9m double-clad multimode Yb:fiber was pumped by a 6W, 975nm multi-mode laser diode. The half-wave plate at the output end was two manifold. Because the dichroic had a broader response with s-polarized light, one use of the half-wave plate was to ensure s-polarized light that allowed the short wavelength to reflect off the dichroic so protect the laser diode. Another use of it was to produce the correct polarization for the maximum grating efficiency.
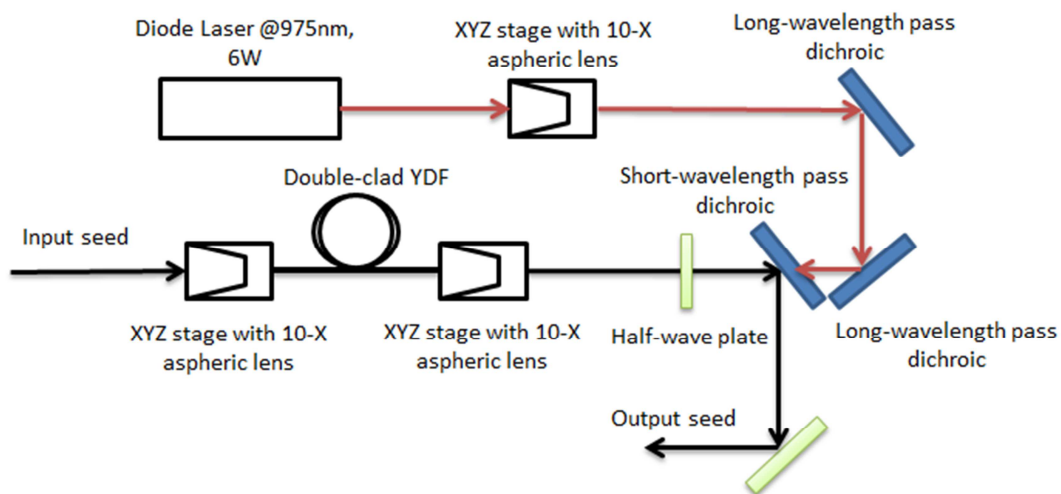

Figure 3-9 The schematic diagram of the third amplifier with 9m double-clad Yb:fiber.

3.5   Grating Compressor

After the three-stage Yb:fiber amplifiers, the two colors need to be compressed to ideally their Fourier transform limited pulse durations. The setup is shown in Figure 3-10. In this grating compressor system, three identical transmission gratings were aligned parallel to each other. The half-wave plate at the third amplifier was used to maximize the diffraction efficiency for the p-polarized transmission gratings. The first grating was also oriented at the 42 degree for the maximum diffraction power and minimum transmission power. The incident beam was sent to the top half of the first grating. The two-color spectrum is diffracted toward the other two gratings, one placed for 1038nm and another one placed for 1103nm. After the two colors are both diffracted by their own gratings, two back mirrors were used to reflect them back to the first grating. The returning beams will hit the bottom half of the first grating and then they finally hit the mirror again but lower than the incident beam. The back mirror b for the long-wavelength color is placed on a translation stage for temporal alignment of the two pulses.

In order to achieve the optimal diffraction angle of the first grating, a power meter was placed at the position of the zero order diffraction of the first grating. By rotating the first grating through its vertical axis, the minimum transmission power can be obtained, which also corresponds to the maximum diffraction efficiency. In addition, the distances between the first grating and the other two gratings need to be determined. It is well known that the spectral frequency-dependent phase shift produced by a dispersive device, such as a grating compressor, can be expressed as in a Taylor expression about a central frequency ω_o :

$$\phi(\omega) = \phi(\omega_o) + \phi_1(\omega - \omega_o) + \phi_2(\omega - \omega_o)^2 + \phi_3(\omega - \omega_o)^3 + \cdots, \qquad (70)$$

where ϕ_1 is the group delay, ϕ_2 is the second order dispersion, and ϕ_3 is the third order dispersion term. According to Treacy's calculation, the second order dispersion or the GDD can be written as (Treacy, 1969)

$$GDD = \phi_2 = \frac{d^2\phi(\omega)}{d\omega^2} = -\frac{l\lambda_o^3}{4\pi c^2 d^2 \left\{1 - (\frac{\lambda_o}{d} - \sin\theta_i)^2\right\}}. \qquad (71)$$

where l is the distance between two gratings, λ_o is the central wavelength of the incident pulse, d is the groove spacing, c is the light speed in vacuum, and θ_i is the angle between the incident pulse and the normal line of the grating. The negative sign shows that the three-grating compressor exhibits a negative dispersion, which makes it possible to compress a positively chirped pulse. Moreover, it is obvious that the compression depends not only on the incident angle, but also on the distance. In our experiment, the proper distance for the two colors was determined by measuring the pulse duration using an intensity autocorrector. Treacy also showed that the sign of the third order dispersion is positive in his paper. Thus, the third order dispersion of the compressor and the third order dispersion of the 100m single mode fiber have the same sign and they will simply add, resulting in pulse broadening. Thus, the experimental setup compressor can just compensate the second order dispersion.
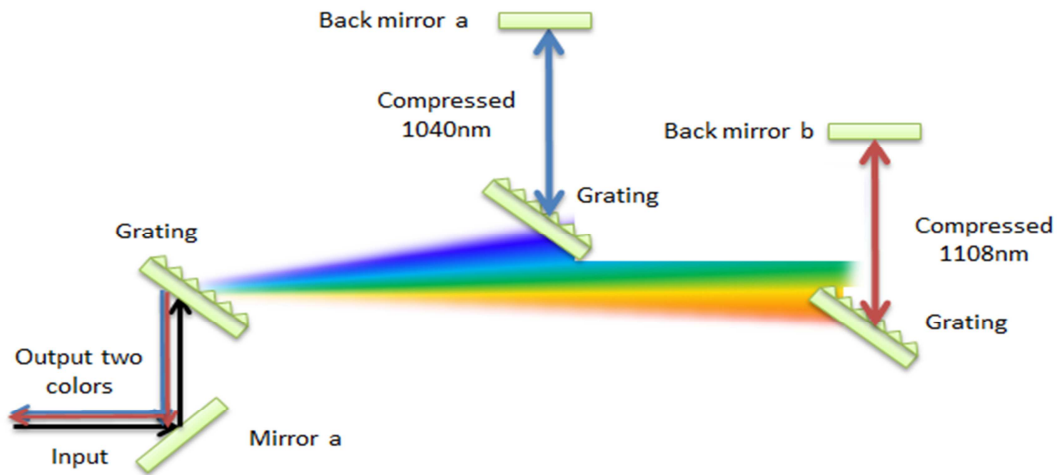
Figure 3-10 The schematic diagram of the grating compressor.

3.6 Mid-Infrared Generation and Conventional MIR Detector

In this section, I used the same experimental setup from our previous work (Al-Kadry, 2011). Figure 3-11 shows the schematic setup for generating and detecting ultrafast MIR pulses. The blue lines represent the path of the short-wavelength pulse, while the red lines represent that of the long-wavelength pulse. Before this setup, we applied a periscope to rotate the red-color beam from s polarization to p polarization. Then the two colors were combined at a polarization beam splitter (PBS) to travel as a single beam. The PBS has a high reflection efficiency for the s-polarized short-wavelength beam, and high transmission efficiency for the p-polarized long-wavelength beam. After that, both beams were sent towards another periscope, which was used to rotate the polarization of the both beams by 90 degree. Thus, after the periscope, the polarization of the short-wavelength beam has been changed to p polarization and that of the long wavelength beam has been rotated to s polarization. A 400mm focal length lens sitting on a translation stage was exploited to focus the combined beams into a 1mm thick GaSe crystal for MIR generation. The reasons why we choose a GaSe crystal as our MIR generation medium are its large second-order nonlinearity, broad transparency range of 0.65μm to 20μm (Abdullaev, 1972), and large birefringence (Vodopyanov, 1999). The GaSe crystal was held in a rotational stage with two degrees of freedom: the azimuthal angle about its optical axis and the phase matching angle through the vertical axis. By carefully rotating those two angles, the phase matching of the difference frequency generation and the maximum MIR generation can be obtained. The generated MIR beam was 1:1 imaged by using a 5cm

focal length spherical gold mirror placed at about 10cm from the crystal. Then a flat gold mirror will send the MIR beam into the detector placed 10cm from the spherical mirror. A Ge filter was placed just in front of the detector to eliminate the incoming two-color beams. The detector here for MIR radiation is a liquid nitrogen cooled HgCdTe (MCT) detector. The weak output signal of the MCT was pre-amplified by a battery-operated operational amplifier (op-amp) by a factor of 1000. The amplified MCT signal was measured using a lock-in amplifier. In order to trigger the lock-in amplifier, a chopping wheel was used to chop the long-wavelength beam with a frequency 1 kHz.
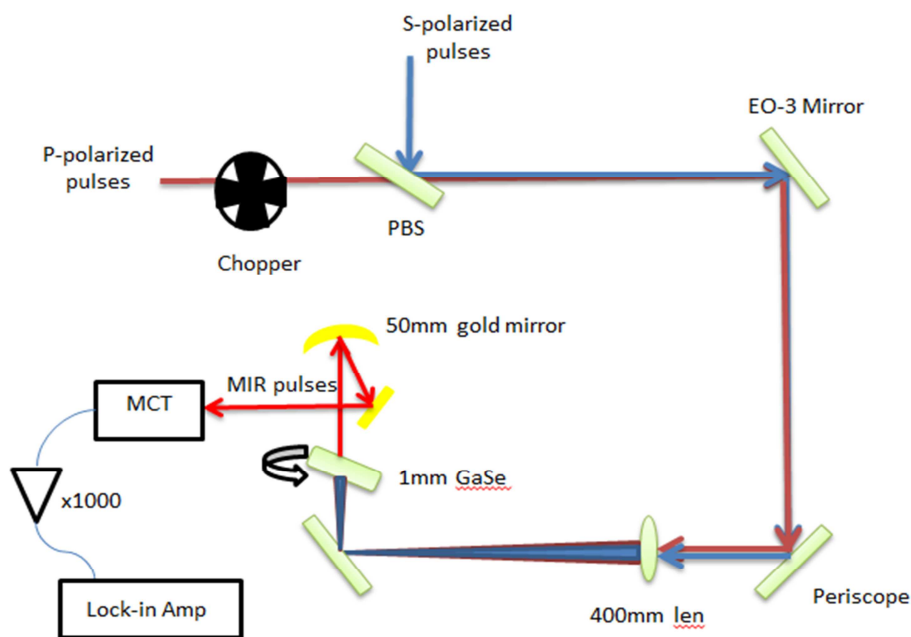
Figure 3-11 The experimental setup of MIR detector by using MCT.

3.7 MIR Detector Based on END-TPA

Based on the large enhancement of the absorption coefficient for END-TPA, a novel sensitive detector using TPA has been setup for detecting the generated MIR radiation centered at 17.6μm. The experimental setup is depicted in Figure 3-12. In this MIR detector, the short wavelength pulses around 920nm (1.347eV) was selected from the super-continuum spectrum by transmission through the short-wavelength pass dichroic mirror used to reflect the longer wavelength to the grating stretcher. In order to eliminate the time delay between the MIR pulse and the 920nm pulse, several large-bandwidth high reflectors were used to delay the 920nm pulse. A corner mirror retroreflector on a translation stage was also used to vary the delay time at the GaAs detector. For the TPA

measurement, a conventional GaAs pin detector with a 0.04mm active diameter was used. Because we need high intensity, the two beams for TPA must be focused very tightly. Thus a 400mm focal lens with 4cm diameter was applied to focus the 920nm beam. According to the datasheet of the GaAs pin detector, it measures the spectral band from 400 to 900nm. The incident beam with wavelength above 920nm cannot be detected by this detector. That is why we will send the 920nm beam and the 17.6μm (0.07eV) beam spatially and temporally together into the detector. This GaAs pin detector was attached to a lock-in amplifier for more sensitive detection of the current signal generated by TPA, and the Lock-in amplifier was trigged by the chopping frequency from a 1-KHz chopper in the 920nm beam.
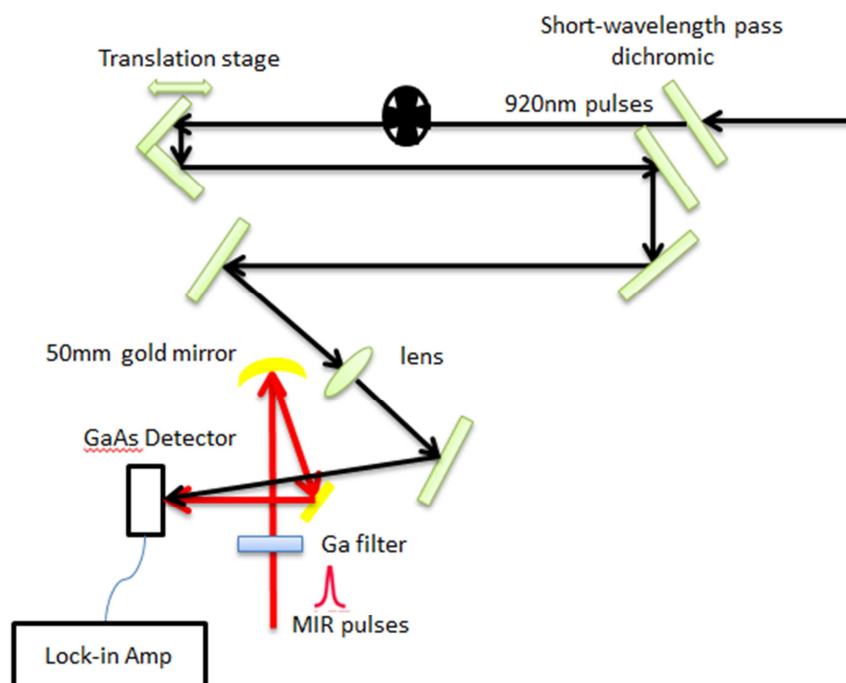

Figure 3-12 The schematic diagram of the MIR detector based on END-TPA.

TPA in the GaAs detector needs two beams focused onto the active area of the detector. The tight beam at 920nm was first sent into the detector without the MIR radiation. Because there is still a small signal at 900nm in the 920nm beam, the lock-in amplifier can measure the weak signal generated by one-photon absorption. By tweaking the mirror just in front of the detector and rotating the detector through its vertical axis, the maximum reading on the panel of the lock-in amplifier can be obtained. Then the second harmonic generation signal from one of the amplified two colors was chopped by the chopping wheel and sent into the active area of the detector.

Because the wavelengths of the SHG signals from the two colors are 519nm and 554nm respectively, they can be easily detected by our GaAs detector. The maximum reading from the lock-in amplifier can also be obtained by tweaking the gold mirror or rotating the GaAs detector. Once both beams fall in the active area of the detector, a Ge filter was applied to eliminate the two intense colors. Because there is walk-off effect for the MIR generation in GaSe, the front gold mirror was needed to tweak again for optimizing the MIR beam. Once the END-TPA happens, the signal can be measured by the lock-in amplifier and the MIR signal will be verified if the signal is gone when blocking either of the two incident beams.

4. Experimental Results and Discussion

In previous works, a two-stage Yb:fiber CPA has been built for MIR generation. Based on this system, Hajialamdari successfully amplified two tunable colors for MIR radiation ranging from 16µm to 20µm. The lower limitation of 16µm is because the ASE became very strong if the two colors were further separated. That is why we built up a three-stage amplifier for amplifying the two colors. In my research on the three-stage Yb:fiber amplifier, three different layouts have been developed and tested. In this chapter, I will show all the results obtained from the three layouts. A very powerful two-color output with more than 2.5W can be generated in our final three-stage Yb:fiber amplifier system. Based on the two-color output power, more powerful MIR radiation can be generated.

For the detection of the MIR radiation, two methods were used. Conventionally, the MIR radiation can be detected and measured by a MCT detector. A thermal power meter was also used for confirm of the reading from the MCT detector. In my thesis, a novel detector was attempted for detecting MIR radiation based on END-TPA.

4.1   Spectrum of Super-Continuum Generation

As mentioned in Chapter 3, the experimental setup of super continuum generation is similar to that in the Al-Kadry work (Al-Kadry, 2011). The beam centered at 1030nm was produced by the oscillator and it was sent into a 2m PCF. This SC-5.0-1040 PCF has a ZDW centered at 1040nm, which is very close to the peak wavelength of the oscillator. This was to generate a spectrum that gives a significant amount of energy at 1103nm, and thus enhance the amplification of this wavelength.
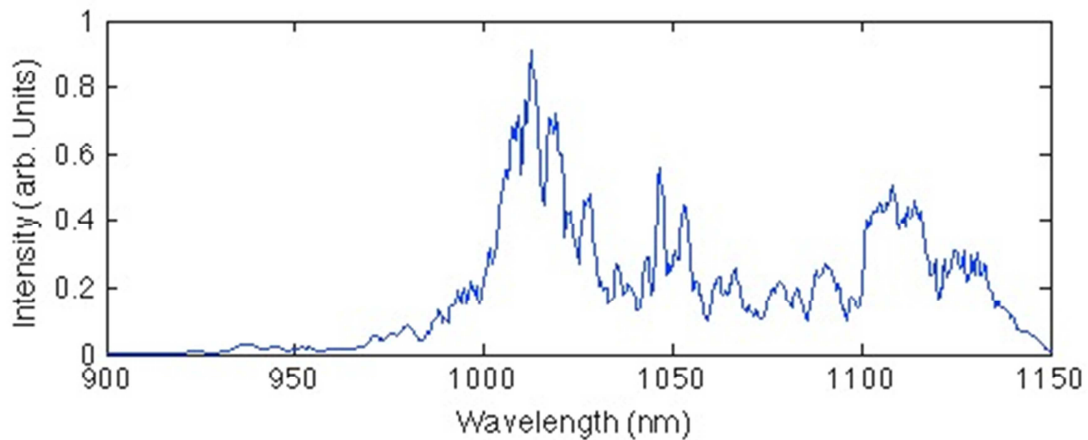
At the output of the super-continuum generation system, the power ranges from 25mW to 27mW. The spectrum will extend from 900nm to 1150nm. By rotating the half-wave plate just before the PCF, the total output power and the super-continuum spectrum can be varied. Figure 4-1 shows the extended spectrum with an output power of 26mW.

From this figure, it is obvious that the spectrum has three peaks centered at 1035nm, 1050nm, and 1105nm. Moreover, most of the power concentrates in the region from 1000nm to 1150nm. However, this spectrum was not obtained at the maximum output power from the PCF. The next figure, Figure 4-2, shows the spectrum of super continuum corresponding to the maximum output power. At this time, the output power is 27mW.

In Figure 4-2, two peaks still centered at 1035nm and 1105nm, but more power from the middle part of the spectrum has shifted to the peaks around 1035nm. All those changes between the two spectra can be obtained by rotating the first half-wave plate just before the PCF.

As the super-continuum generation is so sensitive to the coupling efficiency, small surrounding effects, such as a tiny movement of the mirror from its original position, can change the coupling efficiency of the PCF and thus the output spectrum will be changed. In order to obtain a stable spectrum, the spectrometer was used while tweaking the mirrors and rotating the half-wave plate until a suitable spectrum was obtained with peaks at the two required colors.
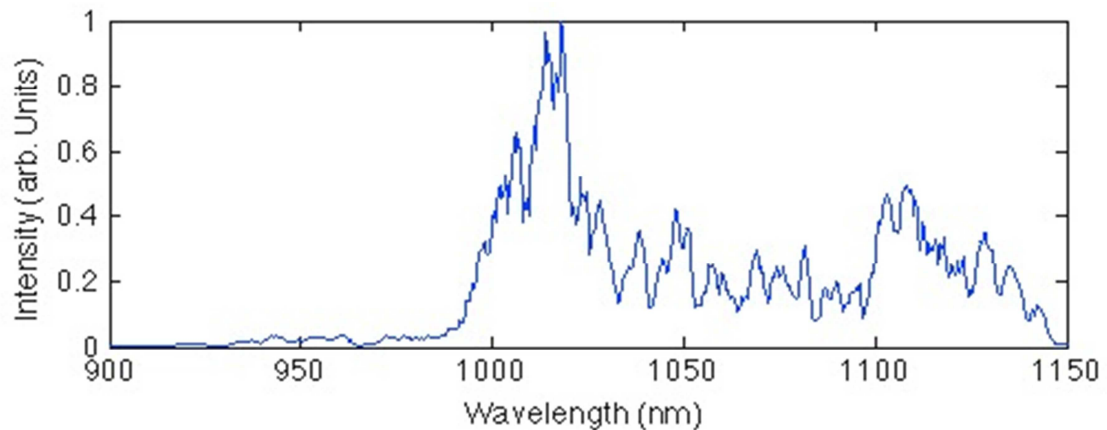
Figure 4-2 The spectrum of super-continuum corresponding to the maximum output from the PCF.

All the three layouts of the three-stage Yb:fiber amplifier included the same setup of the super-continuum generation. Thus all the results from the three different layouts of the amplifier were based on the two colors generated described in this section.

4.2   A Three-Stage Yb:fiber Amplifier with Two Notch Filters and Two Double-Clad Yb:Fiber Amplifiers

In this section, the first layout of the three-stage Yb:fiber CPA is introduced. The continuum generation setup is shown in Figure 3-2. Before the pre-amplifier, two identical notch filters were applied to select the required two colors. Then the two colors were sent to the pre-amplifier, which is shown in Figure 3-5. The second amplification stage is shown in Figure 3-8 but with an 8m-length double-clad highly doped Yb:fiber. As referred to the third amplifier, the experimental setup was the same as shown in Figure 3-9. The general schematic diagram is depicted in Figure 4-3.
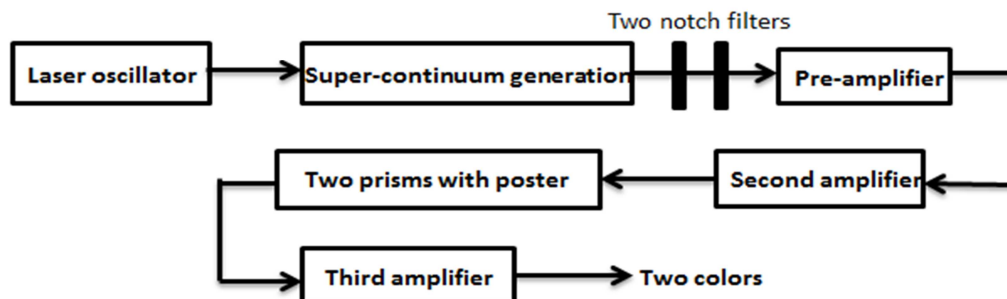

Figure 4-3 The general schematic diagram of the three-stage amplifier with two notch filters.

In Figure 4-3, the two identical notch filters both have a center wavelength at 1064nm, but only a 50nm isolation window. Thus, only one notch filter is not enough to select two colors with a 60nm separation between them. In order to select the two colors with larger separation, we chose two identical notch filters to isolate the unwanted spectrum ranging from 1040nm to 1100nm. One of the notch filters was used to isolate the spectrum above 1040nm and another was used to isolate the spectrum below 1100nm. Both of them can be rotated to change the isolating spectrum region and we obtained the two colors with 60nm separation, which is shown in Figure 4-4. This figure is obtained by rotating the half-wave plate for maximum output power from the super-continuum generation. The 27mW super continuum will drop to 7.6mW after the two notch filters.
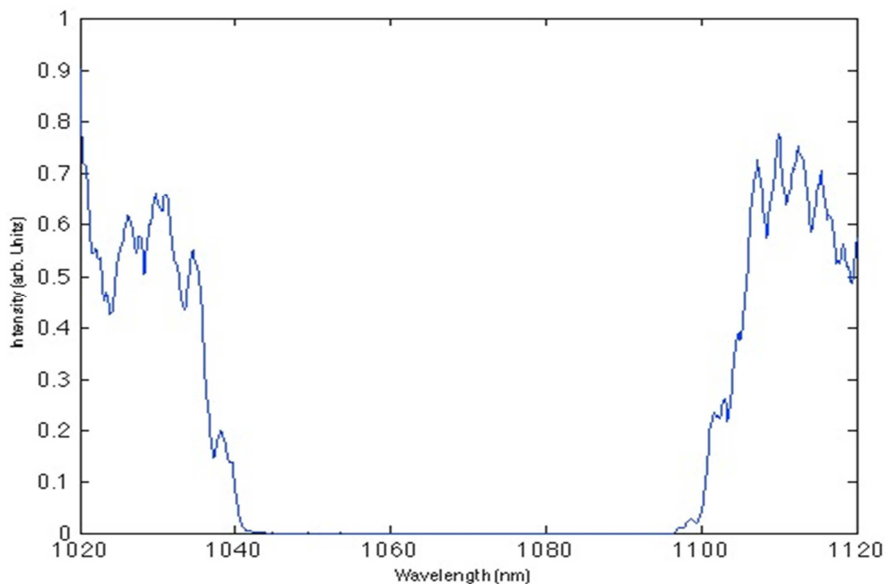

Figure 4-4 The spectrum after two notch filters.

Then the two colors were sent to our pre-amplifier. Two-color spectra after the pre-amplifier are shown in Figure 4-6 and Figure 4-5. Comparing these spectra, both of them have a 60nm separation with small ASE between two required colors. However, the ratio between the blue color and the red color in Figure 4-5 is higher than that in Figure 4-6. This is because the blue color is closer to the peak of the gain in pumped Yb:fibers. When the pump was increased, the blue color can extract more gain from the Yb:fiber. The total output power of the two colors with 200mA pump diode current is 5.8mW, while the power at 220mA is 7.7mW. Under this condition, the pump current of our laser diode has to be turned above 220mA, in order to get output power after the pre-amplifier higher than that incident power of 7.6mW.
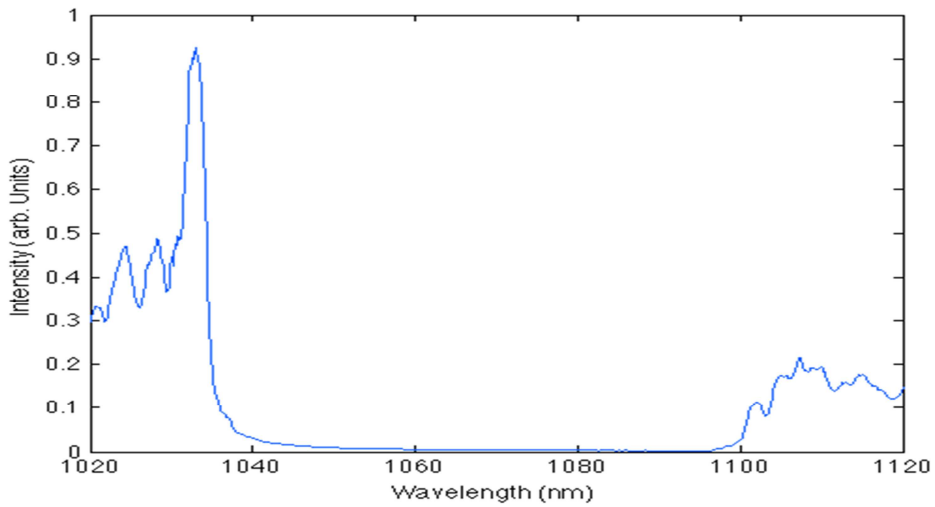
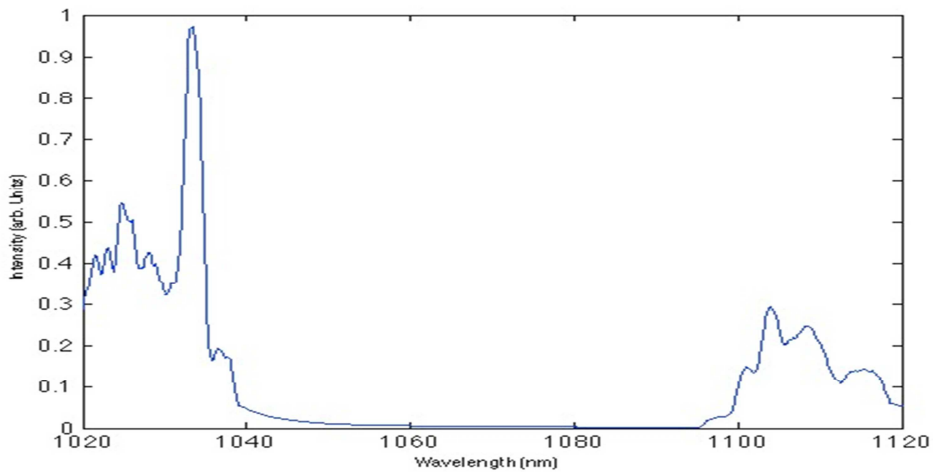**Figure 4-6 The amplified seed after the pre-amplifier at the pump current 200mA.**

Figure 4-5 The amplified seed after the pre-amplifier at the pump current 220mA.

Based on the amplified spectrum of the two colors shown in Figure 4-5, the two colors were further amplified by the second amplifier. Figure 4-8 shows the amplified spectrum of the two colors after the second amplification stage with a pump current of 3.2A. From this figure, we can notice that the seed wavelengths centered at 1038nm and 1103nm have almost the same power. In addition, due to the strong pumping in the second amplifier, the ASE was also produced between 1040nm and

1100nm. Then the multimode diode pump current was turned up to 5.8A, and the output spectrum is shown in Figure 4-7. The output at this pump current can reach up to 119mW. However, the power of the red color is very low, which is not enough to extract enough gain in the next amplification stage. In order to block the strong ASE, we applied two parallel prisms and one post between them
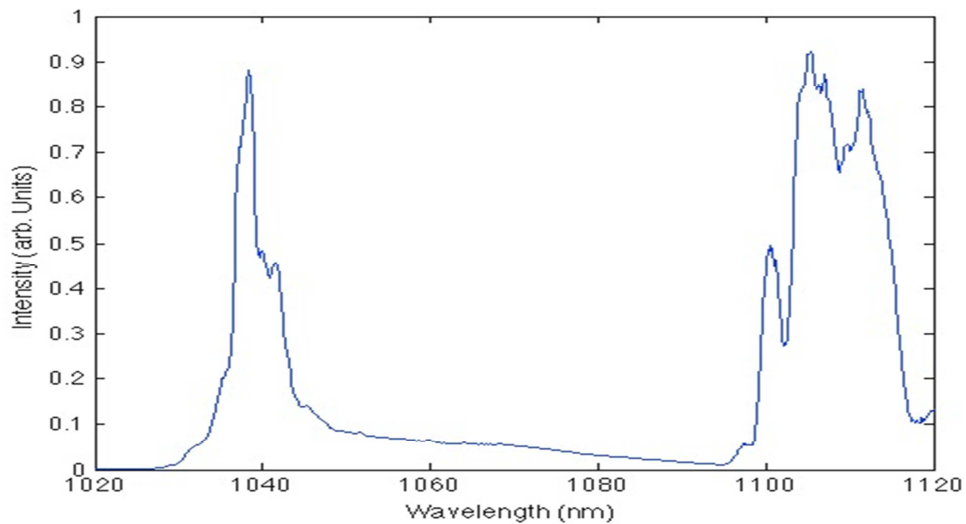

Figure 4-8 The output spectrum after the second amplifier with 3.2A pumping current.
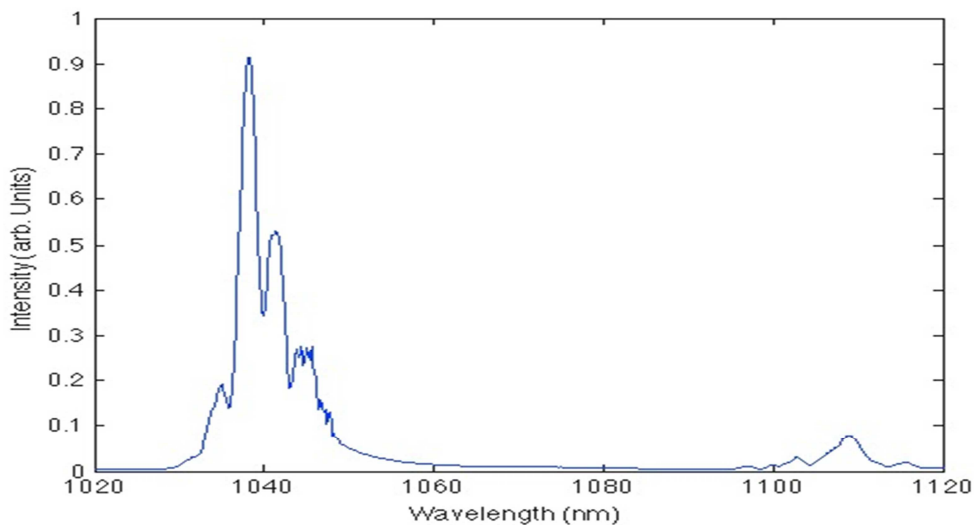

Figure 4-7 The output spectrum after the second amplifier with 5.8A pumping current.

to block the unwanted spectrum between the two required colors. The first prism was used to spatially separate different spectrum elements after the second amplification stage, and a post just before the second prism was used to block the unwanted ASE between the two colors. The second prism collimated the colors and a back mirror was used to reflect the beam back through the prisms to compress the different spectral elements back to the incident circular beam.

48

The post mentioned above was placed on a translation stage and can be moved to block the unwanted spectrum between two required colors. In addition, the two rotatable notch filters before the pre amplifier were rotated to minimize the ASE between 1040nm and 1100nm. The ASE after the second amplifier can be eliminated efficiently by moving the post and rotating the two notch filters. By carefully rotating the first half-wave plate in Figure 3-2 to optimize the ratio of the two colors, the output spectrum after two prisms with a maximum power of 45mW was obtained in Figure 4-9. In this figure, most of the ASE spectrum around 1040nm and 1100nm has been blocked by the post, while transmitting the two colors centered at 1038nm and 1105nm with a 67nm separation were obtained.
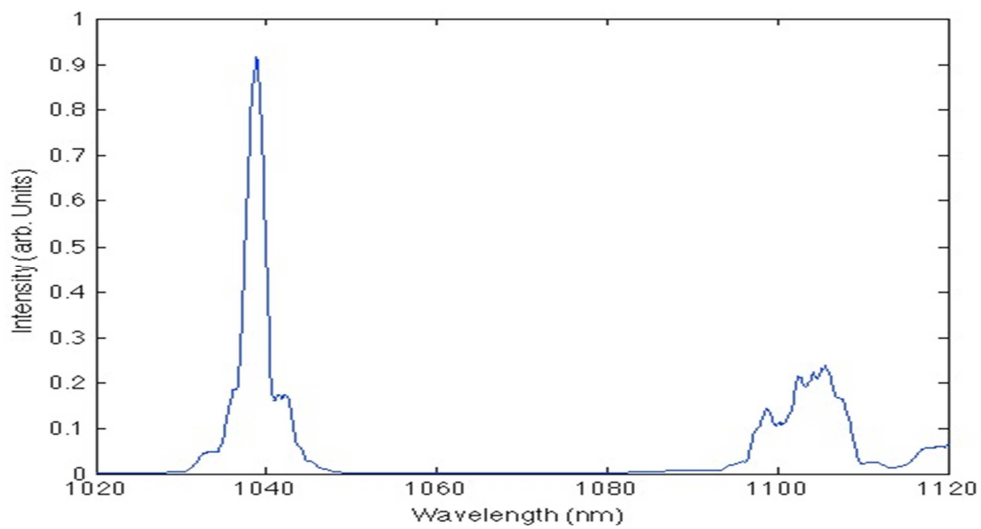

Figure 4-9 The output spectrum with the maximum power after two prisms.

This two-color spectrum was the input seed of the third amplification stage. The output spectrum of the third amplification stage was shown in Figure 4-10.
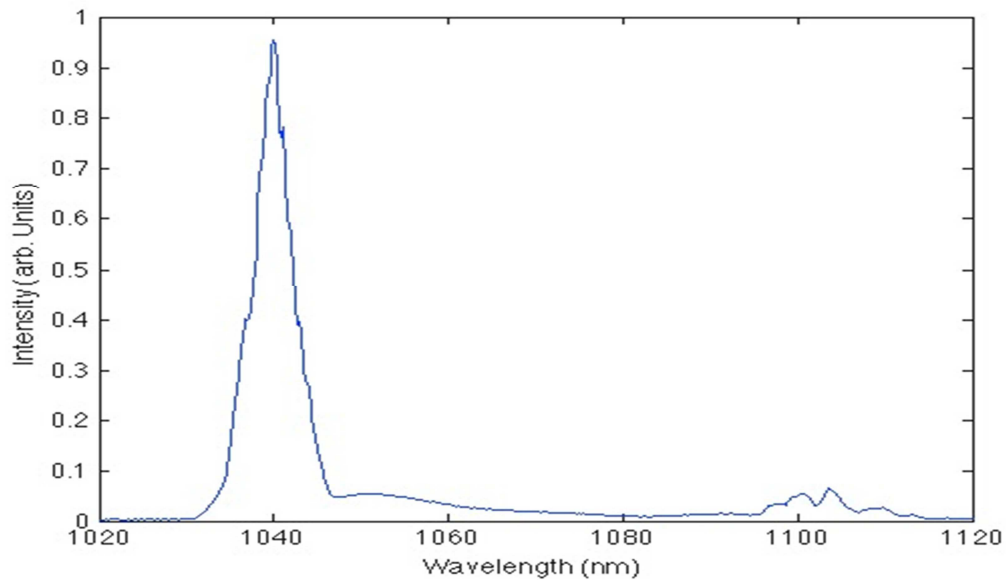

Figure 4-10 The output spectrum after the third amplifier.

From Figure 4-10, the two colors were obtained by turning up the second pump current to 6A and the third pumping current to 5A. There is a 60nm separation between the peak wavelengths of the two colors. However, the peak wavelength of the blue color is shift to 1040nm, because the peak of the gain is centered at 1070nm. The total output power was about 1.1W just after the third amplifier stage. Although there is some unwanted ASE between the two colors, most of the power was concentrated in the blue seed color. The induced ASE can be further eliminated by the compressor for the two colors. As mentioned before, the ultimate goal of my thesis is using the two colors to generate powerful MIR radiation through difference frequency generation. However, the power of the MIR radiation is proportional to the product of powers of the two colors. This output shown in Figure 4-10 cannot generate the required MIR radiation, because the power of the long-wavelength color was too small. Moreover, the 60nm separation between the two colors is not enough to generate MIR radiation with center wavelength around 17.6μm. Thus, the two colors with more power and larger separation in the spectrum needs to be generated by a new three-stage Yb:fiber amplifier system.

4.3 A Three-Stage Yb:fiber Amplifier with the Grating Stretcher and A Second Amplifier Stage Comprised of A Single-Clad Yb:Fiber

In this section, the second layout is introduced. As mentioned before, the total power of the two colors was 7.6mW after the two notch filters. Then the two colors were just amplified to 7.7mW after the pre-amplifier. Due to the low pumping efficiency, we used the grating stretcher as the seed selector, which is shown in Figure 3-3. The two knife edges were used for eliminating unwanted spectra around the two required colors. This also gave us flexibility in selecting the bandwidth of the two colors. We applied the same pre-amplifier setup shown in Figure 3-5. The second amplifier in this layout has been changed and the experimental setup is shown in Figure 3-7. For the third amplifier, we still used the same experimental setup shown in Figure 3-9.

The spectrum after the stretcher is shown in Figure 4-11 with an output power of 2.1mW. A wavelength separation with 60nm can be easily obtained and the total power almost equally distributed between the two colors (1.1mW for blue color and 1mW for red color). The maximum output power can be obtained by rotating the half-wave plate and its spectrum is depicted in Figure 4-12. In this figure, the long-wavelength color has been maximized and the total power is 2.4mW.
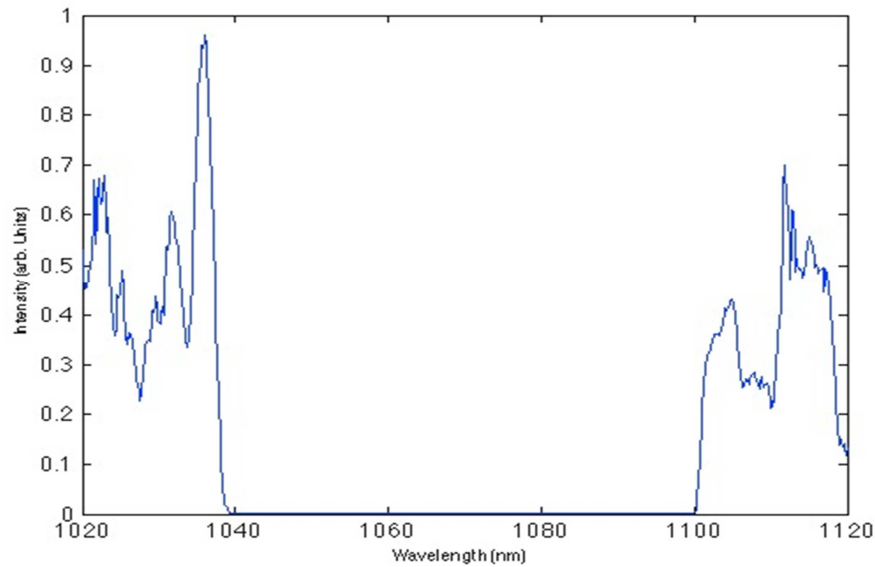
Figure 4-11 The seed after the stretcher with an average power of 2.1mW.
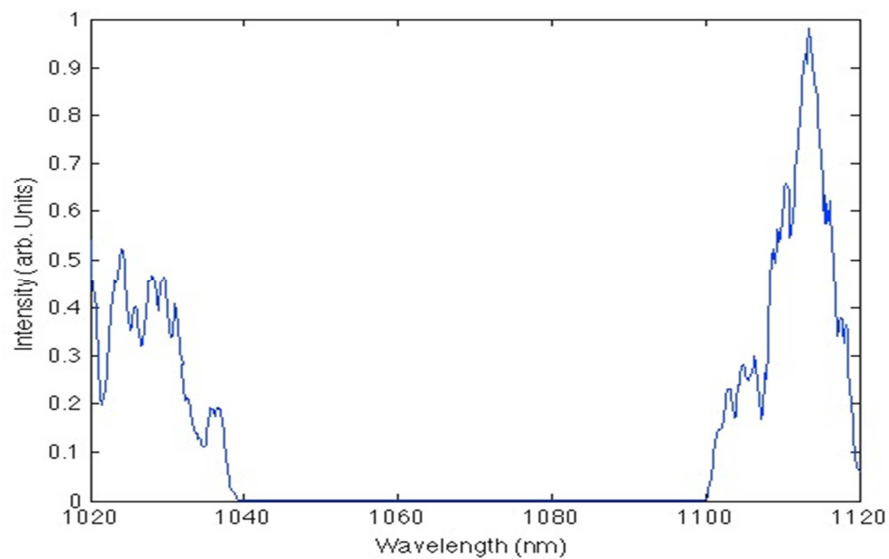

Figure 4-12 The seed after the stretcher with an average power of 2.4mW.

Then the two colors were sent into the same pre-amplifier for amplifying. Without the pumping input, only 30µW blue color can survive from the Yb:fiber with a strong reabsorption at that wavelength range. Most of the output at the end of the pre-amplifier fiber is the red color. However, with the pumping, the 2.4mW incident seed can be pumped to 7.5mW. The amplified spectrum is shown in Figure 4-13. It is obvious that the blue color with center wavelength close to the peak of the gain got more gain than the red color. Most of the 7.5mW output power is the blue color. However, the seed power of 7.5mW is still too small for the competition with the ASE in next main amplifier stage. Thus, we turned up our laser diode of the pre-amplifier to 265mA. The amplified spectrum is shown in

Figure 4-14 with an average output power of 22.6mW. From this figure, the blue color still extracted most of the gain in the Yb:fiber. Comparing with the Figure 4-13 and Figure 4-12, we can also notice that the spectral narrowing of the blue color, which is the result from the spectral shape of the gain in Yb:fiber.
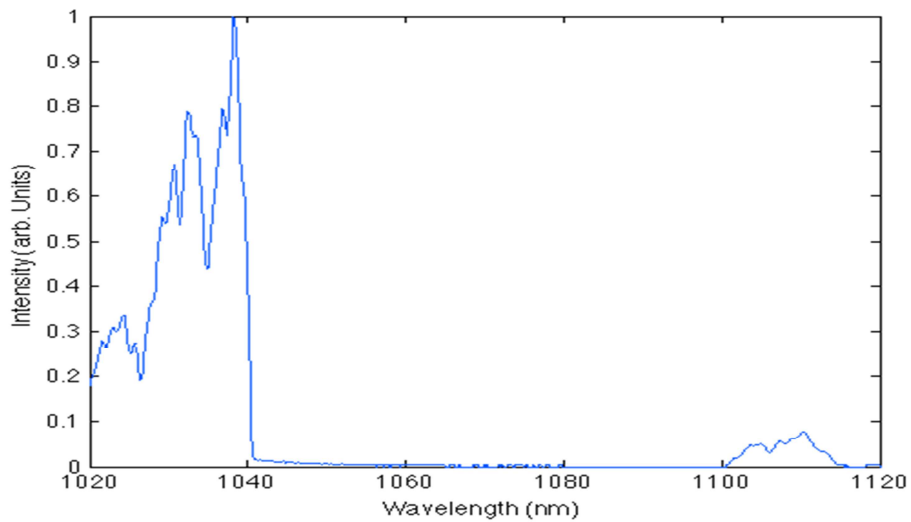

Figure 4-13 The amplified two colors after the pre-amplifier with 200mA pumping current.
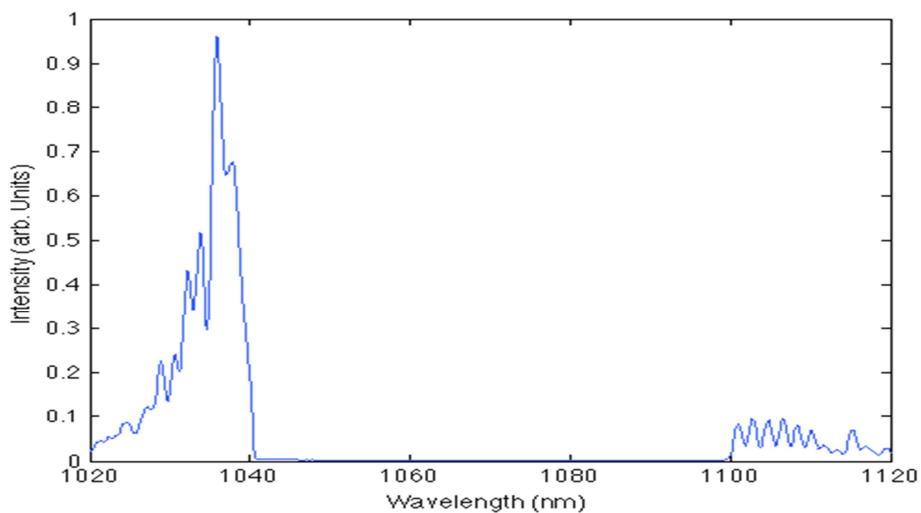

Figure 4-14 The amplified two colors after the pre-amplifier with 265mA pumping current.

Then the amplified two colors were sent to the second amplification stage. To amplify the two colors, the second stage diode pump current was turned to 750mA. Similarly, by rotating the first half-wave plate to maximize the total power, the two colors with maximum total power of 27mW was generated after the two notch filters. The output spectrum is shown in Figure 4-15. In addition, the maximum total power also leads to the maximum long-wavelength-color power. The two notch

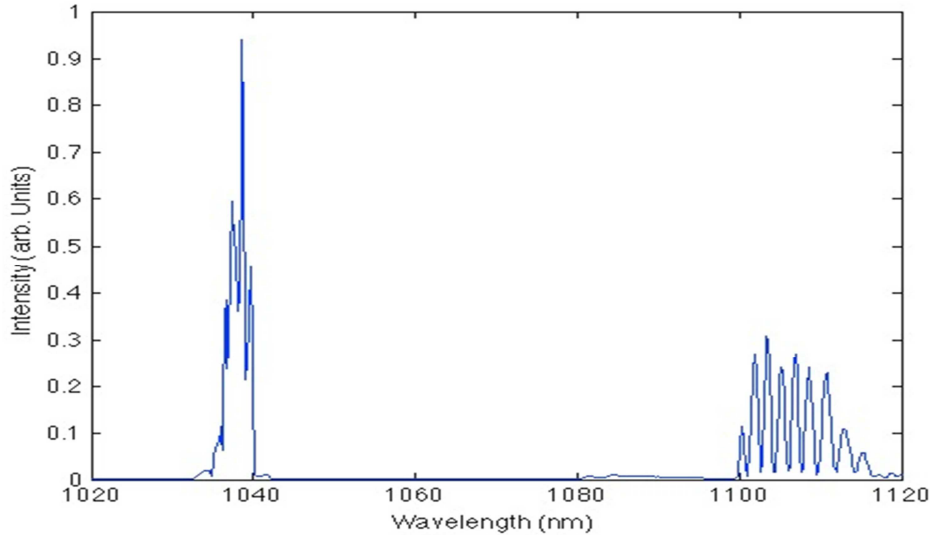filters after the new second amplifier stage were used to block the ASE between the two required two colors.

The two colors shown above were then sent into the same third amplifier mentioned before, and the output spectrum was recorded in Figure 4-17. The pump current of the diode in the third amplifier was turned to 6A to generate the required two colors. It is obvious that the ASE above 1040nm was induced in the pumped Yb:fiber amplifier, which was finally eliminated by the compressor. The measured power after the compressor was 450mW and 60mW for short-wavelength color and long-wavelength color respectively. Compared with the two colors shown in Figure 4-10, the power of the long-wavelength color has been improved, resulting in a better ratio between the short-wavelength color and the long-wavelength color. However, 450mW short-wavelength color was still not strong enough for powerful MIR generation. Due to that limitation, the knife-edges in the stretcher system were moved to let more power around 1040nm incident into the three-stage Yb:fiber amplifier system, a new output spectrum of the two colors was obtained in Figure 4-16. The total power was almost 1.4W for the two colors and the ASE. After the compressor, the short-wavelength color was 800mW and the long-wavelength color was 40mW. Notice that the whole spectrum of the two colors has been shifted to the long-wavelength side, and the two colors centered at 1042nm and 1108nm respectively. The separation between them is approximately 66nm. Compared with the spectra shown in Figure 4-10 and Figure 4-16, the separation between the two colors has been improved and the power of the two colors has been increased.
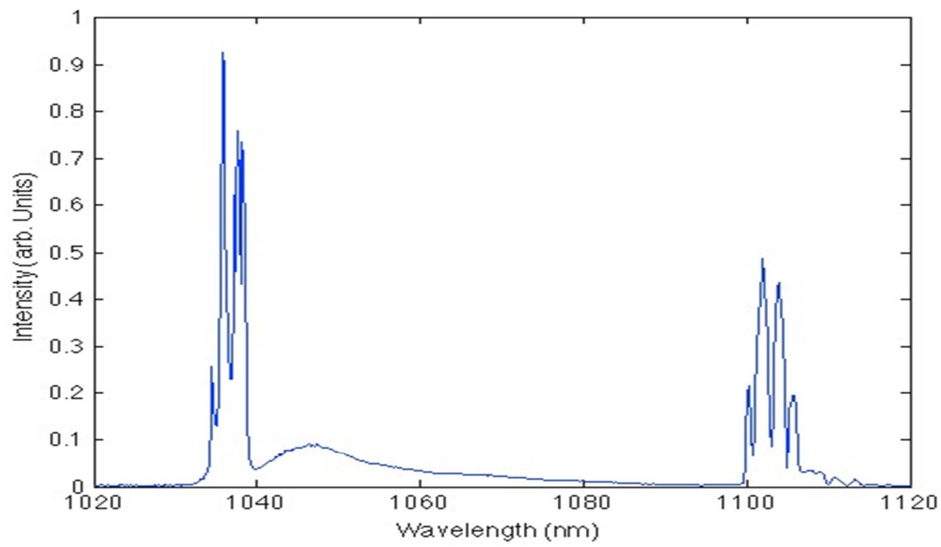
Figure 4-17 The output spectrum after the third amplifier.
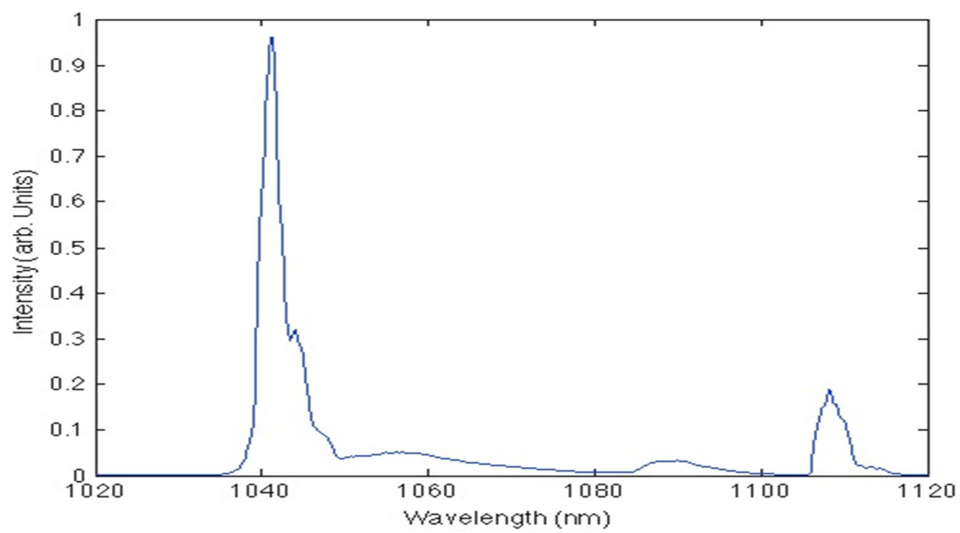

Figure 4-16 Another example of the output spectrum after the third amplifier by moving the knife-edges in stretcher system.

However, the pump current of 750mA was too high for the second pump diode and it died during my experiment. Thus, another three-stage amplifying system needs to be developed for generating more powerful two colors with a larger wavelength separation.

55

4.4 A Three-Stage Yb:Fiber Amplifier with the Grating Stretcher and Two Double-Clad Yb:Fiber Amplifying Stages

In this section, the details of the third layout were introduced. We applied the same grating stretcher for selecting the two colors and the same pre-amplifier to amplify the two colors. For the next two amplifier stages, we used a 5-m-length of double-clad highly doped Yb:fiber for the second amplifying stage, and a 9m length of double-clad highly doped Yb:fiber for the third amplifier. Both of the two stages were pumped by a fiber-coupled multi-mode 975nm diode laser with a maximum average power of 7W in a counter-direction scheme. One notch filter was placed after the second amplifier to eliminate the ASE induced in the second amplification stage. The two colors with total power over 2.5W and 65nm separation were generated at the output end of the third amplifier stage. All the following data were recorded under the condition of generating the maximum MIR radiation.

Figure 4-18 shows the output spectra from the super-continuum generation fiber and after the stretcher. The total power of the super continuum was 26.1mW. After selecting the two colors, the power of the two colors was 2.65mW, with 1.78mW in the short-wavelength color and 0.8mW in the long-wavelength color.
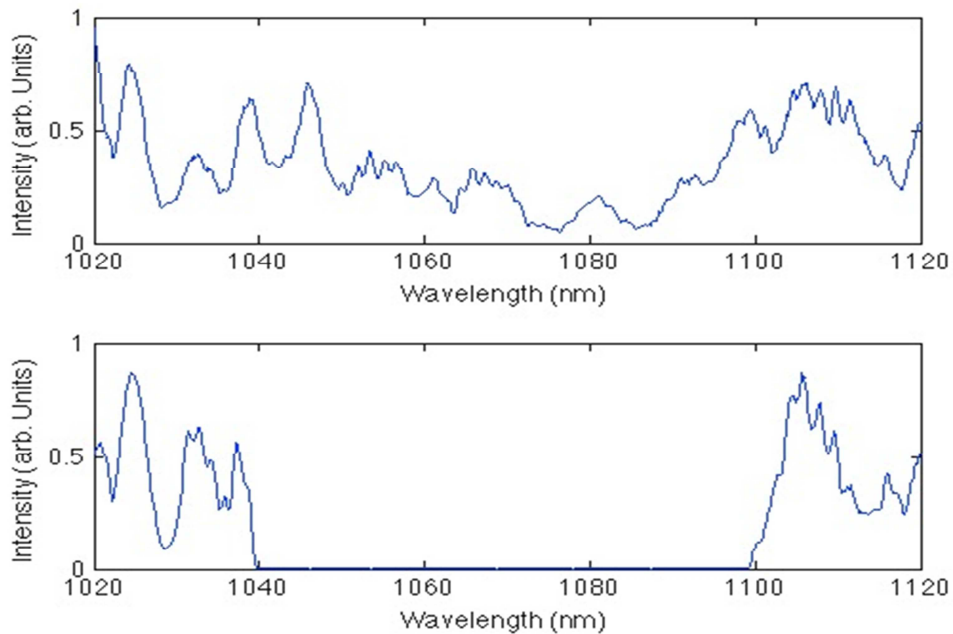

Figure 4-18 The output spectra after the super-continuum generation (top) and the pre-amplifier (bottom).

The two colors with a 60nm separation were sent into the pre-amplifier stage, and the output spectrum is shown in Figure 4-19. The total power of this spectrum was 8.2mW, and most of the power was in the short-wavelength color. This is preferable in the next amplification stage, because the reabsorption was really high for the short-wavelength color in the Yb:fiber. In order to improve the amplification efficiency of the short-wavelength color, it must be strong enough in the pre-amplifier to survive reabsorption in the long Yb:fibers used in the next two amplification stages.
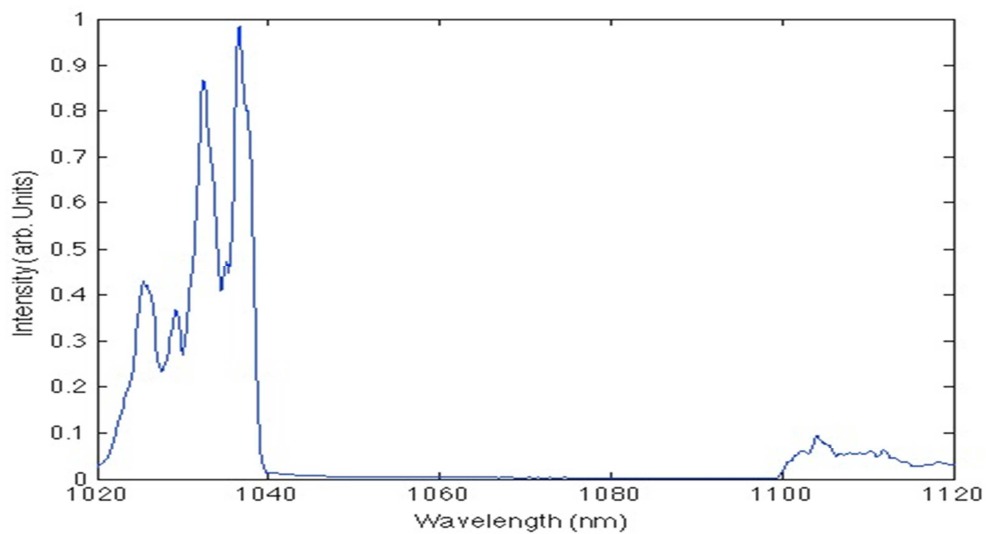

Figure 4-19 The output spectrum after the pre-amplifier with pumping current 265mA.

The output power as a function of the increasing pump current has been plotted in Figure 4-21. This plot shows that the power of the amplified seeds is linearly proportional to the pump current or the pump power. In my thesis, the 2.4mW output from the stretcher has been pumped up to about 9mW with one pump laser diode in a counter direction scheme. The negligible ASE between 1040nm and 1100nm offers us the required two colors with an average power of 9mW to the next amplification stage. Thus, the pre-amplifier not only gives enough power for the short wavelength to boost at the input end of the fiber, but also offers enough gain to the long wavelength to be amplified gradually along the fiber.
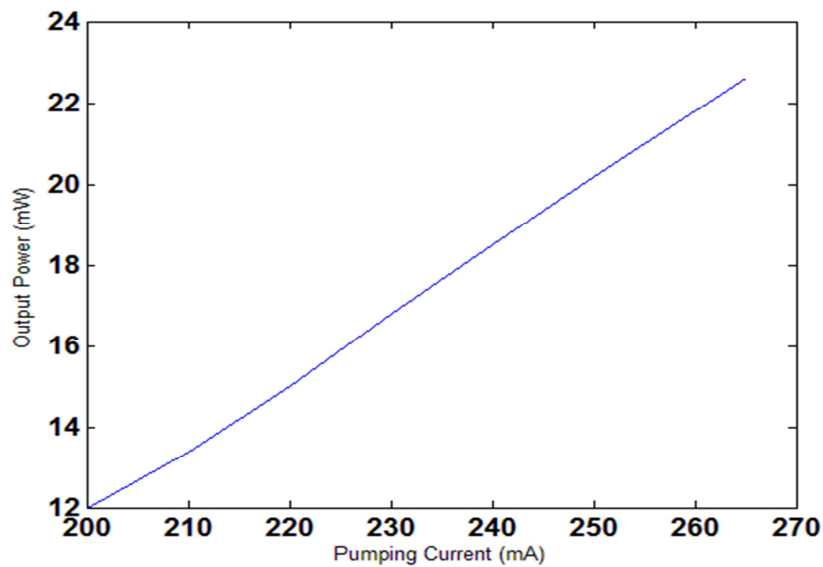
Figure 4-21 The pre-amplifier output power versus the pumping current.

The two colors were further amplified by the second stage. Due to the double-clad Yb:fiber, a powerful multimode laser diode could be used to pump the fiber. Figure 4-20 shows as the pump current or the pump power increases, the output power after the notch filter increases exponentially. This figure also shows that the state of saturation has not been reached in the fiber.

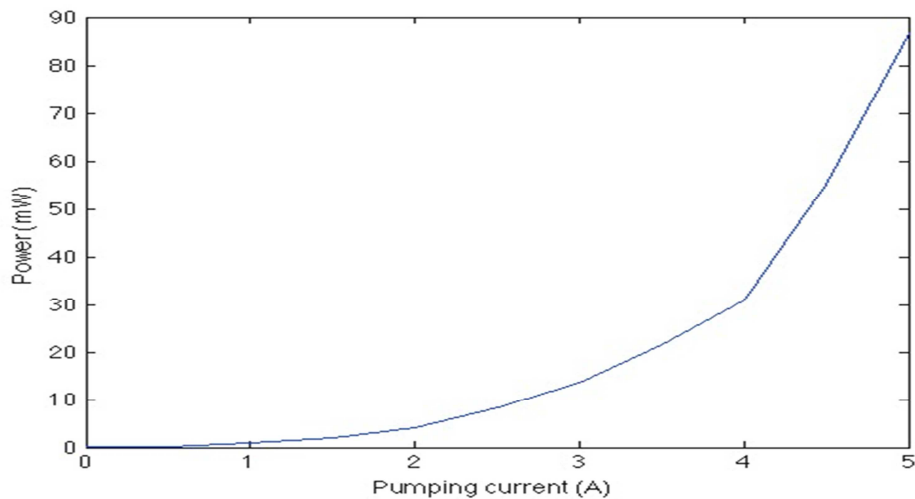**Figure 4-20 The plot of the output seed power versus different pumping current of the second multi-mode diode laser.**

At 5A of the second pump diode, the total power after the second amplifier has already increased to 86.6mW, which was almost three times larger than that obtained in the previous setup. The spectrum after the notch filter is shown in Figure 4-22. In this figure, two colors with a 60nm

separation were obtained. Compared with the previous two colors, the ratio between two colors was almost 2:1 for short-wavelength color over long-wavelength color. The total power was also increased so it can better to compete with the ASE in the next amplification stage.
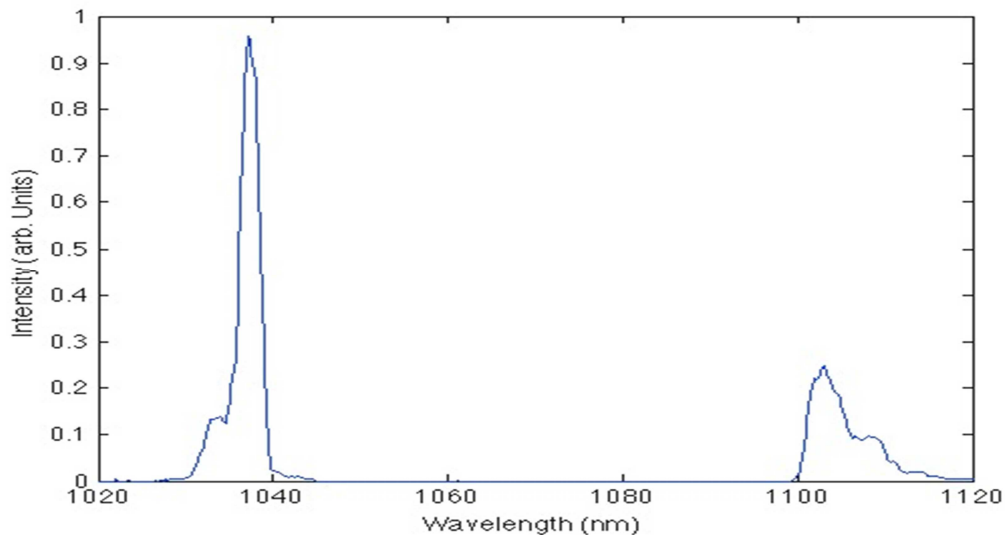

Figure 4-22 The output spectrum after the notch filter with total power of 86.6mW.

Based on the two colors, a longer length Yb:fiber was used for the third amplifier. In order to generate more powerful two colors, the pump current of the third pump diode was turned up to 6.4A. The output spectrum was depicted in Figure 4-23. The peaks of the two colors centered at 1038nm and 1103nm respectively, resulting in a 65nm separation between the two central colors. The total power of the two colors after the third amplifier was 2.65W. Even after the compressor, the powers in the blue color and in the red color were 1.78W and 80mW, respectively. One thing has to be mentioned here is that the actual power of the red color was more than 80mW, and it can be shown from the spectrum in Figure 4-23. The measured power was smaller than the actual power, because our power meter is not sensitive to the longer wavelength beam. These powerful two colors were used to generate powerful MIR radiation around 17.6μm. In addition, both the spectra of each of the two colors have more than 10nm wavelength bandwidth, which means we can further separate the two colors to generate MIR radiation with the peak wavelength lower than 16μm. Compared with the spectrum shown in Figure 4.9 (c) of Hajialamdari's work (Hajialamdari, 2013), the two colors in Figure 4-23 not only have larger power, but also have a better ratio between the two colors. He also mentioned that the further separation was not successful due to the insufficient seed power. The two colors generated from our new three-stage Yb:fiber amplifier were sufficient to separate more than 70nm for MIR radiation.
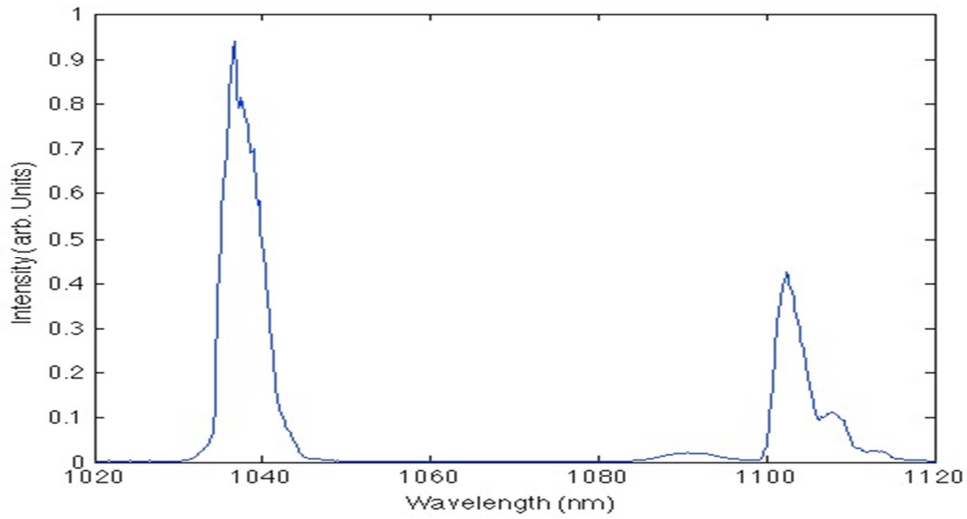
Figure 4-23 The output spectrum after the third amplifying stage with a pump current of 6.4A.

4.5 Two-color Pulse Compression

After generating the two colors from the three-stage Yb:fiber amplifier discussed in Section 4.4, the two colors need to be compressed by applying our compression setup shown in Figure 3-10. In order to obtain the optimal distances of the two second gratings from the first grating in this system, a simple second harmonic generation (SHG) system was applied. According to the SHG theory, the intensity of the output beam is proportional to the square of the intensity of the incident beam. By perfectly compressing the two colors, their SHG should be maximized. The SHG system is shown in Figure 4-24. The two-color beams were focused onto a BBO crystal by a 10cm focal-length lens. The
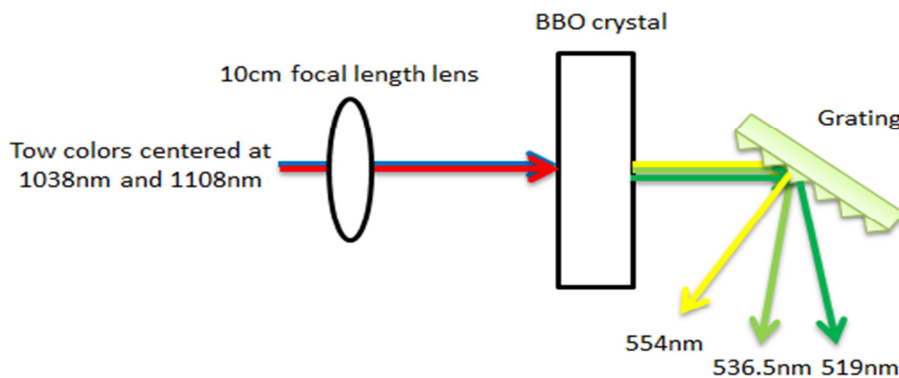

Figure 4-24 The schematic diagram of the SHG of the two colors.

1038nm incident beam can generate the green-color beam with wavelength around 519nm, while

the 1103nm incident beam can generate the yellow-green-color beam with wavelength around 551.5nm. The sum frequency generation (SFG) nonlinear effect in the BBO crystal generated a third beam with wavelength around 535nm given by adding the two input frequencies. Because the three output beams were overlapped with each other, a reflection grating was used to separate them spatially to observe the sum-frequency signal. The distance between the first grating and the second grating of the compressor for the 1038nm beam was optimized to give the maximum SHG signal measured by a power meter. Similarly, the maximum power on the SHG yellow-green light was obtained by changing the compressor length of the red-color compressor arm. The measured maximum power for green light was 9mW, and that for yellow light was approximately 1mW. The back mirrors in Figure 3-10 can be moved back and forward for eliminating the time delay between the two colors, resulting in a maximum power of the 535nm light at the best temporal overlap of the pulses.

Based on this SHG system, the optimal compressor length for 1038nm was 12.7cm and that for 1103nm was 35.6cm. After fixing the two optimal compressor lengths, the two compressed pulses were sent into the autocorrelation for measuring the pulses' durations. With those compressor lengths, the long-wavelength pulse duration was compressed to 610fs, and the short-wavelength pulse duration was compressed to 1.22ps. Because the three-grating compressor cannot correct for the third order dispersion mismatch of the fibers, both pulses were not transform limited.

4.6   Short-Pulse MIR generation

 For MIR generation, we used the same experimental setup from (Al-Kadry, 2011). **Error! Reference source not found.** depicts the schematic diagram of the setup for the ultra-short MIR generation and detection. In order to achieve the most powerful MIR radiation, the perfect phase matching angles of the GaSe crystal needs to be found corresponding to the maximum value measured by the lock-in amplifier. The results of the maximum average power of the generated MIR radiation will also be discussed.

4.6.1   Phase Matching in GaSe

According to the theory of the DFG, the output idler intensity can be written as (Boyd, 2008),

$$I_{MIR} = \frac{8d_{eff}^2 \omega_{MIR}^2 I_p I_s}{n_1 n_2 n_3 \varepsilon_0 c^2} L^2 \, \text{sinc}^2(\frac{\Delta kL}{2}),$$

(72)

where I_p and I_s are the peak intensity of the pump (blue color) and the signal (red color) laser pulses in the nonlinear crystal, d_{eff} is the effective second-order nonlinear optical susceptibility., L is the interaction length in the nonlinear crystal, ε_0 is the permittivity in the free space, c is the speed of light in air, n_1, n_2, and n_3 are the refractive indices of the nonlinear crystal at a certain angle for the idler, pump, and signal radiation respectively, ω_{MIR} is the frequency of the MIR pulse in vacuum, and Δk is the difference between wave vectors. The Δk can be represented as

$$\Delta k = \frac{n_2 \omega_p}{c} - \frac{n_1 \omega_{MIR}}{c} - \frac{n_3 \omega_s}{c} . \tag{73}$$

In order to maximum the peak intensity of the MIR pulses, the Δk needs to be zero in the nonlinear crystal. In my thesis, we use a negative uniaxial crystal GaSe. For GaSe, two types of phase matching are realized by angle tuning (Boyd, 2008), and the two types of perfect phasing matching conditions are shown in Figure 4-25.

$$n_p^e \omega_p = n_s^o \omega_s + n_{MIR}^o \omega_{MIR} \qquad n_p^e \omega_p = n_s^o \omega_s + n_{MIR}^e \omega_{MIR}$$
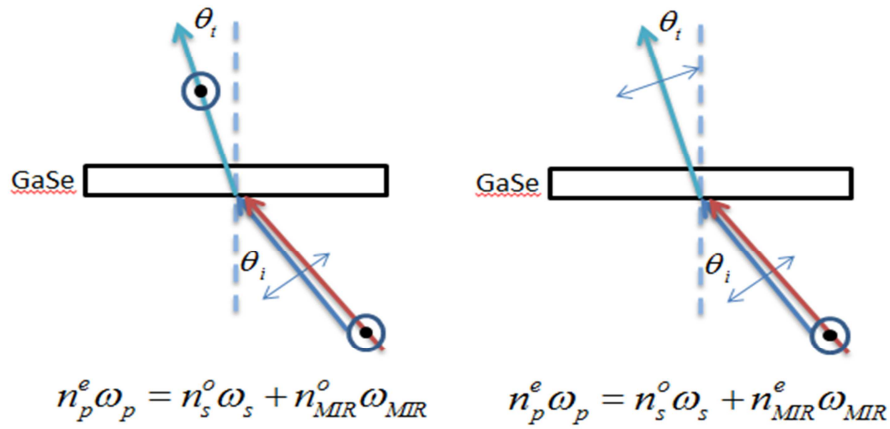
Figure 4-25 The schematic diagram of two types phase matching in GaSe.

As mentioned in Section 3.6, the two colors were orthogonal to each other. In order to achieve phase matching in GaSe crystal, the short-wavelength pulse was s-polarized, while the long-wavelength pulse was rotated by the periscope 90 degree to p-polarized. The s-polarized pulse has a refractive index of $n^e(\theta_t)$ in GaSe crystal, and the refractive index dependents on the angle between the incident beam and the optical axis of the crystal. The long-wavelength pulse has a refractive index of n^o. Thus, by rotating the crystal corresponding to its vertical axis, the above two equations in Figure 4-29 can be accomplished, resulting in perfect phase matching in GaSe crystal. Under that condition,

the maximum MIR radiation can be obtained. Another freedom of the crystal is the azimuthal angle, which can be rotated about its optical axis. This azimuthal angle was used to maximize d_{eff} and it not important for the phase matching (Dmitriev, 1999). The phase matching angle resulting of the maximum MIR radiation was 38^0, which is the angle between the incident beam and the normal line of the crystal surface.

Due to the large walk-off angle of the GaSe crystal, the beam size should be carefully adjusted for optimizing the interaction length in the crystal. Thus, the lens before the crystal was placed on a translation stage for changing the beam sizes on the 1mm thick GaSe. We found that when the 400mm-focal-length focusing lens was placed 43cm away from the crystal, the strongest MIR radiation was obtained.

4.6.2 Results of the Maximum Average Power of the Generated MIR Pulses

A powerful two-color ultrafast spectrum with the peak wavelengths centered at 1038nm and 1103nm was generated by the three-stage Yb:fiber amplifier system. The total power before the compressor was 2.65W. After the compressor, the powers dropped down to 1780mW in the blue color and 80mW in the red color. With the two colors, ultra-short MIR pulses centered at 17.6μm with an average power of 1.7mW was obtained.

The peak wavelength of the MIR radiation was calculated according to the difference frequency theory

$$\lambda_{MIR} = \frac{\lambda_p \bullet \lambda_s}{\lambda_s - \lambda_p},$$

(74)

where λ_s is the peak wavelength of the red color, and λ_p is the peak wavelength of the blue color.

The MIR power was obtained from the calculation based on this center wavelength. From the datasheet of the MCT detector, the responsivity is the maximum with a value of 151mV/mW at the wavelength 22μm, and it will drop to 79.27mV/mW at the wavelength 17.6μm. Because we use a 1mm-thick germanium filter to block the incident powerful two colors, the 30% transmission coefficient at the wavelength 17.6μm has to be considered. When considering the voltage jump at the peak intensity of the ultrafast laser pulses, a maximum average power of the MIR pulses was calculated to be 1.7mW at the central wavelength 17.6μm. Compared with the power obtained by Hajialamdari (Hajialamdari, 2013) at the wavelength 17.6μm (around 0.8mW), the power of MIR

radiation has been increased. The calculation result of the MIR pulses can be verified by the measurement from a thermal power meter. We replaced the MCT detector by the thermal power meter and measured the MIR pulses. After several measurements, the average reading of the thermal power meter was 570μW. By considering the transmission coefficient 30% of the 1mm-thick germanium filter at wavelength 17.6μm, the measured power of MIR radiation was 1.7mW, which was the same as our measurement with the MCT detector.

Figure 4-26 (a) and (b) show the variations of the average power of the 1038nm pulses and the 1103nm pulses as a function of the pumping current of the multi-mode 975nm laser diode in the third amplifier. From (b), we can see that the maximum output power of the long-wavelength color was 110mW, and the output of red color was in the saturated regime. However, the output power of the blue color is in the unsaturated regime, and it can be increased further by increasing the pumping current. The (c) shows the power production of the two colors varies as a function of the pumping current. It is also obvious that the production power of the two colors can be increased, resulting in a more powerful MIR radiation, by increasing the pumping current.
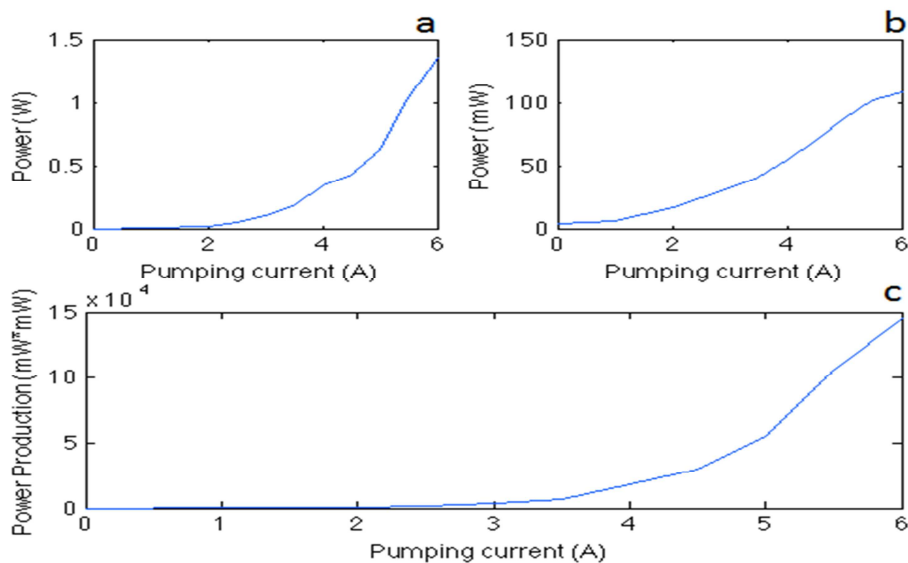
Figure 4-26 Variations of (a) P_1, (b) P_2, and (c) $P_1 \times P_2$ as a function of launched pumping current into the third amplifier.

In my thesis, I did not show the tuning ability of this new system for generating MIR radiation. However, the two spectrally wide pulses shown in Figure 4-27 with a 65nm separation have more power than that shown in Hajialamdari's work. They are also strong enough to be separated further to generate MIR pulses with the peak wavelength lower than 16μm. The central wavelengths of the

two colors actually are tunable via moving the knife edges in the grating stretcher. Having fixed the new central wavelengths of the two colors, all the half-wave plate are adjusted to maximize the average power of the two colors. The grating distances in the compressor also need to be adjusted to minimize the pulse width of the two colors.

4.7   END-TPA in GaAs Detector

The experimental setup of END-TPA is shown in Figure 3-12. In order to obtain the best detection efficiency of the GaAs detector, we placed the GaAs detector on a rotational stage. It is obvious that there is an incident angle between the 920nm pulse and the MIR pulse. This is allowed because the TPA does not need the phase matching of the two incident beams. Once two incident beams are focused in the active area of the GaAs detector, the END-TPA can happen. Because the GaAs detector has a detection range from 400nm to 900nm, we replaced the GaSe crystal in Figure 3-11 by a BBO crystal. When the 1038nm beam was focused on the BBO crystal, the second harmonic generation happened and the green light at 519nm was generated. Then the GaAs detector was rotated to have the maximum reading on the lock-in amplifier. Then the beam at 920nm was sent the GaAs detector by tweaking the large-bandwidth high reflector. The maximum measured power after the short-wavelength pass dichroic in Figure 3-3 was 1.2mW for the 920nm pulse. After the translation stage and several high reflectors, the power at 920nm dropped to 0.9mW before the GaAs Detector. Two beams were both focused tightly, because we want to improve the intensity of the two beams.

The maximum MIR radiation at 17.6μm with power of 1.7mW was generated through our three-stage Yb:fiber amplifier and sent to the detector together with the 920nm beam. Then the translation stage was moved back and forward to eliminate the temporal delay between two beams. However, this experiment was not successful due to the low power at the 920nm beam. In the future, the 920nm pulse needs to be amplified in a semiconductor optical amplifier. In addition, the 920nm pulse has to be recompressed by two parallel gratings, because it has been stretched by the 100m-length single mode fiber in Figure 3-2. Based on this more powerful ultra-short 920 pulse, the pulse duration of the MIR radiation can be measured by this END-TPA detector.

5. Conclusion

In this thesis, a three-stage dual-wavelength Yb:fiber chirped pulse amplifier has been developed. The two colors with 60nm separation were originally generated by a 2-m-length photonic crystal fiber and then selected by the grating stretcher. A three-stage configuration, one with single-clad Yb:fiber and the other two with double-clad Yb:fiber amplifiers, was developed to produce more powerful two-color seed compared with our previous two-stage amplifying system. The pre-amplifier was pumped by a single-mode diode laser centered at 975nm, while the other two main amplifiers were pumped by two identical multi-mode diode lasers with a maximum average power of 6W centered at 975nm. The total average power of the two colors after this three-stage amplifier was increased to 2.65W, and a 65nm separation between the two colors was obtained at the same time. A compressor containing three gratings was used to recompress the two colors. Due to the fact that the compressor was not able to compensate the higher order dispersion in fibers, the amplified two colors were compressed to 610fs and 1220fs, respectively.

The MIR radiation generation was implemented in a 1-mm-thick GaSe crystal. A maximum average power of 1.7mW was obtained at 17.6μm by difference frequency mixing the dual-wavelength pulses with the peak wavelengths of 1038nm and 1103nm with average powers of 1780mW and 80mW respectively. This power was measured by the MCT detector, and confirmed by a thermal power meter. In order to measure the pulse duration of the MIR radiation, the MIR pulse was sent to a GaAs detector together with the short-wavelength pulse centered at 920nm. However, the experiment of END-TPA in GaAs was not successful and the 920nm beam needs to be amplified in the future.

References

Abdullaev, G. B., Kulevskii, L. A., Prokhorov, A. M., Savel'Ev, A. D., Salaev, E. Y., & Smirnov, V. V. (1972). GaSe, a new effective material for nonlinear optics.JETP Lett., 16(3), 90-95.

Al-Kadry, A. M., & Strickland, D. (2011). Generation of 400 µW at 17.5 µm using a two-color Yb fiber chirped pulse amplifier. Optics letters, 36(7), 1080-1082.

Alfano, R. R. (2006). The Supercontinuum Laser Source: Fundamentals with Updated References, 568 pp.

Boyd, R. W. (2008). Nonlinear Optics, Third Edition. Academic Press.

Cirloganu, C. M., Padilha, L. A., Fishman, D. A., Webster, S., Hagan, D. J., & Van Stryland, E. W. (2011). Extremely nondegenerate two-photon absorption in direct-gap semiconductors [Invited]. Optics express, 19(23), 22951-22960.

Diels, J. C., & Rudolph, W. (2006). Ultrashort laser pulse phenomena. Academic press. Ebrahim-Zadeh, M., & Sorokina, I. T. (Eds.). (2008). Mid-infrared coherent sources and applications. Springer.

Dmitriev, V. G., Gurzadyan, G. G., & Nikogosyan, D. N. Handbook of Nonlinear Optical Crystals, 1999. Springer Series in Optical Sciences, Springer, Berlin, ISBN 3540653945.

Dumon, P., Priem, G., Nunes, L. R., Bogaerts, W., Van Thourhout, D., Bienstman, P., ... & Baets, R. (2006). Linear and nonlinear nanophotonic devices based on silicon-on-insulator wire waveguides. Japanese journal of applied physics, 45(8S), 6589

Dunn, M. H., & Ebrahimzadeh, M. (1999). Parametric generation of tunable light from continuous-wave to femtosecond pulses. Science, 286(5444), 1513-1517.

Ehret, S., & Schneider, H. (1998). Generation of subpicosecond infrared pulses tunable between 5.2 µm and 18 µm at a repetition rate of 76 MHz. Applied Physics B: Lasers and Optics, 66(1), 27-30.

Fishman, D. A., Cirloganu, C. M., Webster, S., Padilha, L. A., Monroe, M., Hagan, D. J., & Van Stryland, E. W. (2011). Sensitive mid-infrared detection in wide-bandgap semiconductors using extreme non-degenerate two-photon absorption. Nature Photonics, 5(9), 561-565.

Galvanauskas, A., Cho, G. C., Hariharan, A., Fermann, M. E., & Harter, D. (2001). Generation of high energy femtosecond pulses in multimode-core Yb-fiber chirped-pulse amplification systems. Optics letters, 26(12), 935-937.

Hajialamdari, M., Alkadry, A. M., & Strickland, D. (2011). Modeling of a two-color, two-stage, ultrafast Yb-doped fiber amplifier. Optics Communications,284(12), 2843-2848.

Hajialamdari, M., & Strickland, D. (2012). Tunable mid-infrared source from an ultrafast two-color Yb: fiber chirped-pulse amplifier. Optics letters, 37(17), 3570-3572.

Hajialamdari, M. (2013). Tunable Two-Color Ultrafast Yb: Fiber Chirped Pulse Amplifier: Modeling, Experiment, and Application in Tunable Short-Pulse Mid-Infrared Generation (Doctoral dissertation, University of Waterloo).

Hegenbarth, R., Steinmann, A., Sarkisov, S., & Giessen, H. (2012). Milliwatt-level mid-infrared (10.5–16.5 μm) difference frequency generation with a femtosecond dual-signal-wavelength optical parametric oscillator. Optics letters,37(17), 3513-3515.

Hutchings, D. C., & Van Stryland, E. W. (1992). Nondegenerate two-photon absorption in zinc blende semiconductors. JOSA B, 9(11), 2065-2074.

Kaiser, W., & Garrett, C. G. B. (1961). Two-Photon Excitation in Ca F 2: Eu 2+.Physical Review Letters, 7(6), 229.

Martinez, O. E. (1987). 3000 times grating compressor with positive group velocity dispersion: Application to fiber compensation in 1.3-1.6 μm region.Quantum Electronics, IEEE Journal of, 23(1), 59-64.

Paschotta, R., Nilsson, J., Tropper, A. C., & Hanna, D. C. (1997). Ytterbium-doped fiber amplifiers. IEEE journal of Quantum Electronics, 33(7), 1049-1056.

Romero-Alvarez, R., Pettus, R., Wu, Z., & Strickland, D. (2008). Two-color fiber amplifier for short-pulse, mid-infrared generation. Optics letters, 33(10), 1065-1067.

Sheik-Bahae, M., Hutchings, D. C., Hagan, D. J., & Van Stryland, E. W. (1991). Dispersion of bound electron nonlinear refraction in solids. Quantum Electronics, IEEE Journal of, 27(6), 1296-1309.

Silfvast, W. T. (2004). Laser fundamentals. Cambridge University Press.

Strickland, D., & Mourou, G. (1985). Compression of amplified chirped optical pulses. Optics communications, 55(6), 447-449.

Treacy, E. (1969). Optical pulse compression with diffraction gratings. Quantum Electronics, IEEE Journal of, 5(9), 454-458.

Van Stryland, E. W., Woodall, M. A., Vanherzeele, H., & Soileau, M. J. (1985). Energy band-gap dependence of two-photon absorption. Optics letters, 10(10), 490-492.

Vodopyanov, K. L. (1999). Mid-infrared optical parametric generator with extra-wide (3–19-µm) tunability: applications for spectroscopy of two-dimensional electrons in quantum wells. JOSA B, 16(9), 1579-1586.Yariv, A., & Yeh, P. (2006). Photonics: Optical Electronics in Modern Communications (The Oxford Series in Electrical and Computer Engineering). Oxford University Press, Inc..

Weiner, A. (2011). Ultrafast optics (Vol. 72). John Wiley & Sons.

Wherrett, B. S. (1984). Scaling rules for multiphoton interband absorption in semiconductors. JOSA B, 1(1), 67-72.